Review

Hoon Yeub Jeong, Eunsongyi Lee, Soo-Chan An, Yeonsoo Lim and Young Chul Jun*

3D and 4D printing for optics and metaphotonics

https://doi.org/10.1515/nanoph-2019-0483
Received November 26, 2019; revised January 4, 2020; accepted January 7, 2020

Abstract: Three-dimensional (3D) printing is a new paradigm in customized manufacturing and allows the fabrication of complex optical components and metaphotonic structures that are difficult to realize via traditional methods. Conventional lithography techniques are usually limited to planar patterning, but 3D printing can allow the fabrication and integration of complex shapes or multiple parts along the out-of-plane direction. Additionally, 3D printing can allow printing on curved surfaces. Four-dimensional (4D) printing adds active, responsive functions to 3D-printed structures and provides new avenues for active, reconfigurable optical and microwave structures. This review introduces recent developments in 3D and 4D printing, with emphasis on topics that are interesting for the nanophotonics and metaphotonics communities. In this article, we have first discussed functional materials for 3D and 4D printing. Then, we have presented the various designs and applications of 3D and 4D printing in the optical, terahertz, and microwave domains. 3D printing can be ideal for customized, nonconventional optical components and complex metaphotonic structures. Furthermore, with various printable smart materials, 4D printing might provide a unique platform for active and reconfigurable structures. Therefore, 3D and 4D printing can introduce unprecedented opportunities in optics and metaphotonics and may have applications in freeform optics, integrated optical and optoelectronic devices, displays, optical sensors, antennas, active and tunable photonic devices, and biomedicine. Abundant new opportunities exist for exploration.

Keywords: 3D printing; 4D printing; functionalized ink; smart materials; optical components; metaphotonic structures.

1 Introduction

Three-dimensional (3D) printing is a new paradigm in the customized manufacturing of products and components using digital blueprints [1–3]. In contrast to traditional subtractive manufacturing methods, an arbitrary 3D object can be built layer-by-layer from the bottom up; thus, this technique is also referred to as additive manufacturing. 3D digital objects can be realized with unprecedented complexities in shape and material. Various materials, such as polymers, ceramics, composites, and metal powders, have been used in 3D printing. 3D printing is employed in various fields, including automotive and aerospace [4, 5], microfluidics [6, 7], bioengineering [8, 9], and medicine [10].

Figure 1 shows different types of conventional 3D printing methods, and Table 1 presents their main features. Fused deposition modeling (FDM) is a common type of 3D printing that is widely used in either low-cost 3D printers or professional 3D printers. It is based on the material extrusion, where thermoplastic materials are melted and pulled out through a nozzle to form successive object layers. PolyJet 3D printing is based on the material jetting, where liquid photopolymers are dropped and cured with ultraviolet (UV) light. The cured layers are built one-by-one to create a complete 3D object. Direct ink writing (DIW) is an ink-based technique, where ink can be extracted from a nozzle, like a fluid, because of low viscosity with applied shear stress. The printed structure can maintain its shape owing to high viscosity in the absence of shear stress. Stereolithography (SLA) involves the formation of a solidified component from a liquid bed via laser illumination. Laser light cures photopolymers and the exposed portion of the polymers hardens with each pass over the object. After each pass, the built plate or platform moves down slightly until the intended 3D structure is completed. A digital light processing (DLP) is used in DLP 3D printing to expose each and entire layer all at once, and thus DLP can enable large printing volumes

*Corresponding author: Young Chul Jun, School of Materials Science and Engineering, Ulsan National Institute of Science and Technology (UNIST), Ulsan 44919, Republic of Korea, e-mail: ycjun@unist.ac.kr. https://orcid.org/0000-0002-7578-8811
Hoon Yeub Jeong, Eunsongyi Lee, Soo-Chan An and Yeonsoo Lim: School of Materials Science and Engineering, Ulsan National Institute of Science and Technology (UNIST), Ulsan 44919, Republic of Korea

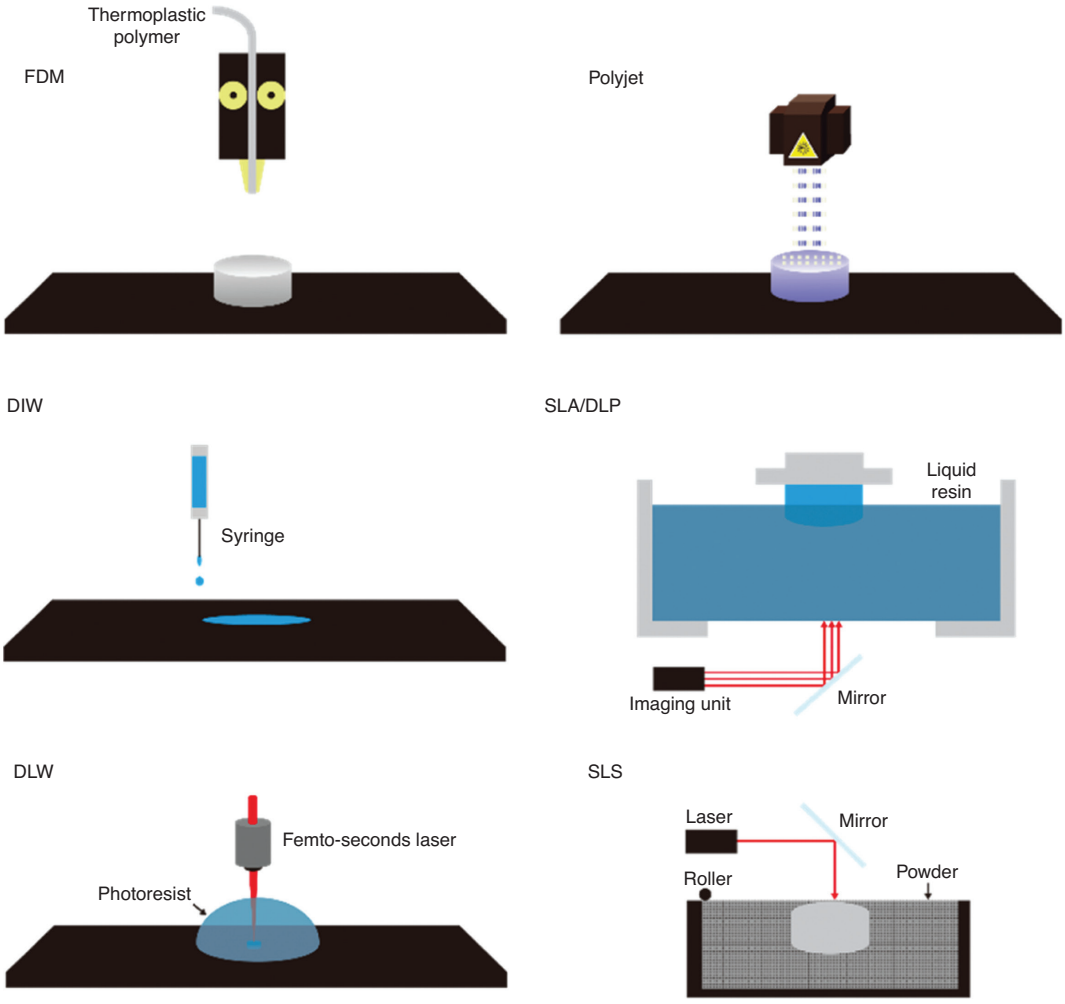

Figure 1: Schematics of the 3D printing methods: Fused deposition modeling (FDM), PolyJet (or Material jetting), Direct ink writing (DIW), Stereolithography (SLA)/Digital light projector (DLP), Direct laser writing (DLW), Selective Laser Sintering (SLS).

Table 1: Comparison of 3D printing methods.

Printing method	Materials	Advantages	Disadvantages
FDM	Thermoplastic polymers	Simple Cheap	Low resolution Roughness issue Limitation in complexity
PolyJet (material jetting)	Photocurable polymer	Multi-material Smooth surface High quality	High cost
DIW	Polymers, ceramics	Diverse material Versatility	Low resolution Fragile Post curing
SLA/DLP	Photocurable resin	Smooth surface Recyclable raw material	Single material Limited material Resin absorbs moisture
DLW	Photoresist Photocurable polymer	High resolution No need for support	High cost Limited material Time consuming
SLS	Metal powder, ceramic powder, polymer powder	No need for support Recyclable raw material High quality	Roughness issue High cost Post processing

at high speed. Direct laser writing (DLW) uses nonlinear multi-photon absorption induced by ultrafast laser pulses to increase the resolution. Metal powders and ceramic powders are commonly used in selective laser sintering (SLS), where the powder is piled up layer-by-layer and laser sintering is performed to create metal or ceramic 3D structures.

3D printing has been also employed for the fabrication of complex optical components and metaphotonic structures. Conventional lithography techniques (such as photolithography and electron-beam lithography) are usually limited to planar, two-dimensional (2D) patterning. However, 3D printing can allow the fabrication of complex 3D shapes and multiple parts without post-assembly. 3D-printed optical components can be interconnected along the out-of-plane direction, which is extremely difficult for traditional planar (2D) patterning techniques. Additionally, 3D printing can allow printing on nonplanar surfaces or curvilinear substrates. Furthermore, it allows a high level of customization and reduces the amount of material waste in production. Moreover, 3D printing can be useful for fabricating metaphotonic structures. Metaphotonics offers unprecedented control of electromagnetic fields in engineered materials and structures, in a manner not achievable with conventional optics [11]. Therefore, metaphotonics often require non-conventional, complex 3D structures.

While 3D printing normally produces static structures with fixed shapes and functions, four-dimensional (4D) printing adds active, responsive functions to 3D-printed structures (the additional dimension is time *t*) [12, 13]. 4D-printed structures are also called "programmable matter"; a response can be programmed into materials via structural and compositional design. 4D printing can be realized by using smart materials that respond to environmental stimuli, such as heat, moisture, pH, chemical species, and electric or magnetic fields. Therefore, using 4D printing, the shape or properties of structures created via 3D printing can be transformed in response to external stimuli. These active structures can be useful for a wide range of potential applications in actuators, switches, sensors, deployable structures, soft robotics, and medical devices.

Four dimensional printing concept was introduced by Tibbits [14]. They demonstrated a 3D-printed self-folding structure; this printed structure was initially a one-dimensional rod, but when immersed in water, the structure was transformed into a 3D structure, because of the swelling of polymers in water. 4D printing research is being further accelerated with the rapid development of multi-material 3D printing. Multi-material printing can provide a venue for realizing various active structures. Based on multi-material 3D printing, there have been various studies on multi-functional structures and sequentially deforming or actuating structures [15–18]. For example, Le Duigou et al. fabricated a bio-inspired electro-thermo-hygro reversible shape-changing structure using a hygroscopic polyamide matrix and continuous carbon fibers [19]. Mao et al. fabricated sequential self-folding structures using different shape-memory polymers (SMPs) [20]. 4D printing can also be applied to soft robots to remove complex sensors or electric circuits. Chen et al. fabricated soft untethered robots that can propel to a desired direction in water [21]. To obtain the driving force to propel a soft robot, they introduced a bistable fin structure; the fin structure snapped to another stable state rapidly in water, and the soft robot was propelled in the target direction. Additionally, 4D printing can be applied to active optical and microwave structures.

In this paper, we have presented a variety of recent developments in 3D and 4D printing with regard to applications in optics and metaphotonics. This review focuses on topics that are interesting for the nanophotonics and metaphotonics communities. In Section 2, we have discussed functional materials for 3D and 4D printing. We first introduced 3D printing filaments and inks that include nanoparticles or conductive materials inside. Then, we have discussed smart materials for 4D printing. In Section 3, we have presented various designs and applications of 3D and 4D printing in the optical, terahertz (THz), and microwave domains. Lastly, we have concluded with future perspectives in Section 4.

2 Functional materials for 3D and 4D printing

2.1 3D printing with embedded functional nanoparticles

3D printing requires novel materials to enhance the functionalities of printed structures. However, the available materials for 3D printing are limited, because of the requirements for printing; e.g. materials with appropriate shear stress are needed to maintain the shape during DIW, and transparent materials are needed for photopolymerization in SLA. In this regard, mixing functional nanoparticles with conventional 3D printing materials can be a viable option to enhance the optical functionalities of printed structures. There have been several reports on 3D

printing with embedded functional nanoparticles, such as plasmonic metal nanoparticles, quantum dots (QDs), and luminescent dye molecules.

Figure 2 shows several examples of functional structures with selective light absorption or emission. Figure 2A–C show metal nanoparticles with different sizes [22]. Silver nanoprisms exhibit higher plasmonic sensitivity than spherical nanoparticles (Figure 2A) and have advantages for sensing and filtering applications. The nanoprism absorption peak is very sensitive to their size (15–80 nm) and covers almost the whole visible region. Therefore, silver nanoprisms exhibit various colors depending on their size (Figure 2B and C). These nanoprisms were mixed with conventional printing materials [Pluronic F-127 and poly(ethylene glycol) diacrylate (PEGDA)] to create 3D-printed colored structures with discrete color grading (Figure 2D) and continuous color grading (Figure 2E). By controlling the syringe pressure, different nanoparticle distributions (either discrete or continuous) were obtained via 3D printing.

Semiconductor QDs can emit light at different wavelengths (i.e. different colors), because of the size-dependent quantum confinement effect. Figure 2F shows a fully 3D-printed QD light-emitting diode (QD-LED) on a contact lens [23]. The QD emission layer was printed via DIW together with multiple other layers. A 3D-printed orange-red QD-LED on a non-flat contact lens exhibited good electrical characteristics (Figure 2G). Because 3D printing can be performed on curved surfaces as well as flat planes, 3D-printed QD-LEDs are promising for many novel applications. Luminescent dyes were also employed for 3D printing [24]. Figure 2H shows 3D-printed structures under UV lamp illumination. These 3D structures were printed with embedded luminescent dyes: Rhodamine B (red color), Solvent Yellow 98 (green color), and BBOT (blue color). Complex luminescent structures were printed with DLP using luminescent photopolymer resins. Various colors were obtained by blending two or more resins (Figure 2I).

2.2 Conductive filaments and inks for microwave antennas and components

Conductors are very effective for generating and confining electromagnetic waves and thus are essential for many microwave antennas and components. However, the conventional fabrication methods for microwave

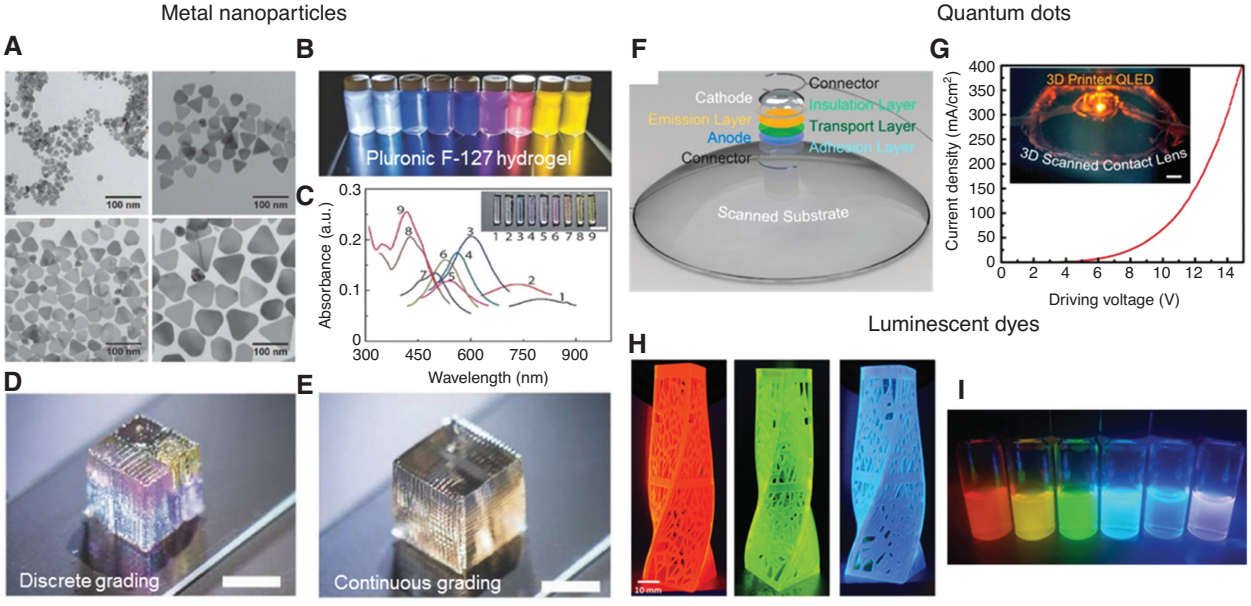

Figure 2: 3D printing with functional nanomaterials.
(A) TEM images of different sizes (15, 39, 58, 79 nm) of silver nanoprisms. (B) Photograph of Pluronic F-127 plasmonic inks with different sizes of silver nanoprisms. (C) Absorbance spectra (Inset shows the printed inks, scale bar: 5 mm). (D) Photograph of a discretely functionally graded 3D-printed plasmonic cube. (E) Photograph of a continuously functionally graded 3D printed plasmonic cube (scale bars: 5 mm). Adapted from Ref. [22]. Copyright (2017) John Wiley & Sons. (F) Schematic showing the QD-LED components printed on a curved surface. (G) Graph of current density vs. voltage of the 3D-printed QD-LED on a contact lens. The inset exhibits the electroluminescence from the 3D-printed QD-LED (scale bar: 1 mm). Reprinted from Ref. [23]. Copyright (2014) ACS Publications. (H) DLP printed complicated vases under the UV light illumination, which show luminescent red, green, and blue colors. (I) Photograph of the different luminescent color resins by blending. Reprinted from Ref. [24]. Copyright (2017) John Wiley & Sons.

components often involve multiple processing steps (such as metal deposition, etching, and micromachining), as well as post-integration. 3D printing of conductive materials can be a viable alternative; conductive composite filaments and inks that include carbon materials (graphite, carbon black, etc. [25]) or metal particles as fillers in a polymer matrix can provide sufficient conductivity for many practical applications. In particular, 3D printing of such composite materials is promising for lightweight, flexible microwave components. Additionally, for enhancing the design flexibility or functionality, it is possible to control or gradually vary the dielectric permittivity by using several filaments together or dynamically mixing inks. Moreover, 3D printing can allow the direct printing of complex structures without micromachining.

Figure 3 shows the several examples of 3D-printed microwave antennas and components. Figure 3A shows a flexible, lightweight bowtie antenna [26]. It was 3D-printed using conductive acrylonitrile butadiene styrene (ABS) as an antenna material (black part in the figure) and PLA as a substrate (red part in the figure). Then, the printed antenna was attached to an SMA connector using conductive glue. The bowtie antenna exhibited a good return loss in the frequency range of 6.8–8.7 GHz (corresponding to a relative bandwidth of 24%) (Figure 3B). Additionally, using conductive filaments that included copper particles, 3D printing of Mills cross cavity antennas was demonstrated for computational microwave imaging [27]. Figure 3C shows the receiving (left) and transmitting (right) cavities. In the antenna, slot-shaped unit cells have rectangular slots for

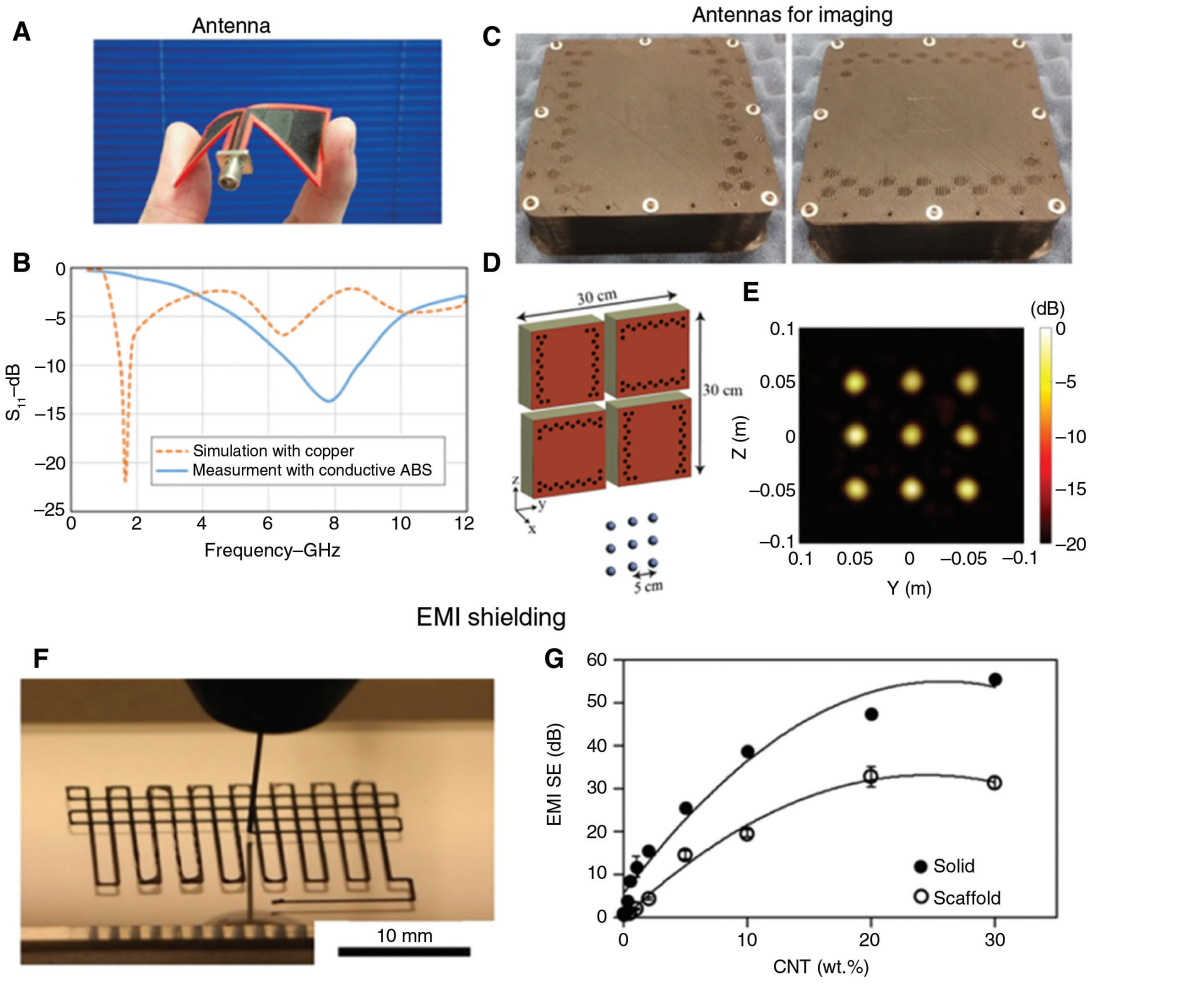

Figure 3: Conductive materials for microwave applications.
(A) Photograph of a 3D-printed antenna. (B) Reflection coefficient spectrum of the 3D-printed antenna. Reprinted from Ref. [26]. Copyright (2015) IEEE. (C) Picture of 3D-printed Mills-Cross cavity antennas. The left side is a receiving cavity and the right one is a transmitting cavity. (D) Synthesized composite apertures for imaging of a point-scatter array. (E) Reconstructed image of the array by the computational imaging algorithm. Reprinted from Ref. [27]. Copyright (2017) IEEE. (F) 3D printing of conductive scaffolds using a CNT/PLA solvent. (G) Graph of averaged EMI SE of the solid (i.e. filled) and scaffold patterns with different CNT loadings in the X-band range. Reprinted from Ref. [28]. Copyright (2017) Elsevier.

single-polarization imaging with varying lengths for the flattening of the radiation response in the K-band region. Using information collected from antennas with swept frequency, original images were reconstructed via computational imaging algorithms (Figure 3D and E).

Electromagnetic interference (EMI) shielding was demonstrated using conductive inks, where carbon nanotubes (CNTs) were mixed with a PLA matrix and dissolved in a dichloromethane (DCM) solvent [28]. Conductive patterns were 3D-printed using a micronozzle and then solidified rapidly via the volatile DCM solvent (Figure 3F). This method was denoted as solvent-cast 3D printing. In contrast to 3D printing of solid filaments with high filler contents, it was free from clogging in the nozzle, because of the low viscosity of the conductive inks dissolved in the solvent. With the increasing CNT content, the EMI shielding effectiveness (SE) increased up to 30 dB (corresponding to 0.1% transmission) for a patterned scaffold with an inter-filament spacing of 0.7 mm (Figure 3G). Additionally, this EMI shielding pattern maintained visible-region transparency of >40%. Thus, conductive-ink patterns can provide effective shielding of microwave signals while maintaining substantial transparency to the human eye.

2.3 Smart materials for 4D printing

3D printing of smart materials that are responsive to external stimuli (such as heat, moisture, electric/magnetic fields, and pH) is called 4D printing (the fourth dimension is time). In this case, 3D-printed structures are no longer static; rather, their shapes or functionalities can transform over time (Figure 4A). More information regarding general 4D printing research can be found in recent reviews [34–37]. In this section, we have provided more details on stimuli-responsive, smart materials that have been widely employed for 4D-printing studies: SMPs, hydrogels, and liquid crystal elastomers (LCEs).

The 4D printing of SMPs involves 3D printing of an original shape, followed by thermomechanical programming. During thermomechanical programming, the printed SMP structure is deformed into a temporary shape above the glass-transition temperature T_g and then cooled

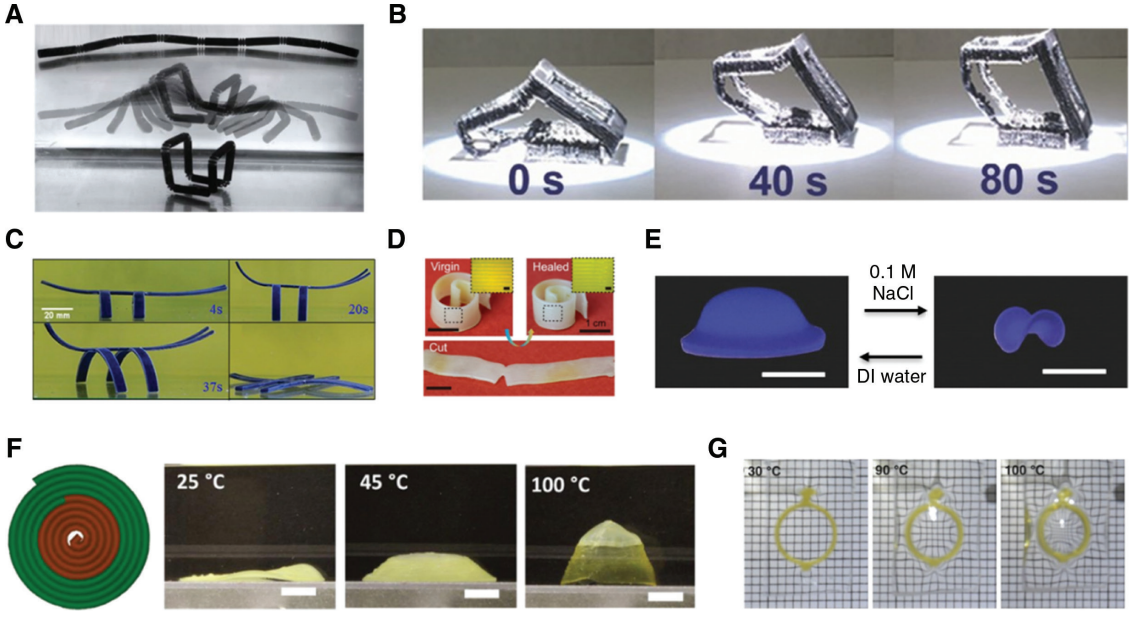

Figure 4: 4D printing with smart materials.
(A) 4D-printed structure that transforms its shape from a 1D line to a 3D cube. Adapted from Ref. [14]. Copyright (2014) John Wiley & Sons. (B) The shape memory process of the cubic frame made of carbon black doped polyurethane under light illumination of 87 mW/cm^2. Adapted from Ref. [29]. Copyright (2017) John Wiley & Sons. Copyright (2016) Nature Publishing group. (C) 3D-printed structure that is mimicking the insect. The deformation behavior of the structure in a 30°C water is shown over time. The image on the lower right corner is the fully recovered structure in the 60°C water. Adapted from Ref. [16]. (D) Photographs of the shape memory assisted self-healing effect. Inserted pictures are the optical microscope images with a scale bar of 1 mm. Adapted from Ref. [30]. Copyright (2018) ACS Publications. (E) Hydrogel based 4D-printed structure (scale bar: 1 cm). Adapted from Ref. [31]. Copyright (2017) John Wiley & Sons. (F) Sequential deformation of a multi-material LCE structure. With molecular engineering, different actuation temperatures were realized (scale bar: 5 mm). Adapted from Ref. [32]. Copyright (2019) John Wiley & Sons. (G) 4D-printed structure that combined LCE with PDMS for adaptive optics. The pictures show the grid observed at different temperatures. Adapted from Ref. [33]. Copyright (2018) John Wiley & Sons.

back to room temperature to fix the temporary shape. When it is heated again above the T_g, the original permanent shape is recovered. SMPs can be easily used in conventional 3D printing methods, such as FDM and PolyJet. Thermoplastic SMPs such as PLA [38, 39] and thermoplastic polyurethane [29, 40, 41] can be used in FDM 3D printing. For example, Yang et al. fabricated photoresponsive 3D-printed structures using polyurethane filaments that included carbon black [29] (Figure 4B). Owing to the high efficiency of the photothermal conversion of carbon black, the programmed structures returned to their original shapes under light illumination (even under sunlight). In the PolyJet method, UV-curable SMPs [13, 16, 42] such as photocurable polyurethane can be used. For example, Wu et al. fabricated multi-shape active composites with photocurable polyurethane-based SMPs [16] (Figure 4C). By combining several SMPs with different T_g values and rubber-like printing materials, a 4D-printed structure was demonstrated that had different shapes at different temperatures. SMPs have been also used in other 3D-printing methods. Zarek et al. created SMP structures for flexible electronic devices using SLA [43]. Conductive ink printing was combined with SMP structures to define electrical contacts. With electrical Joule heating, an electrical conduction path was formed via the shape-memory function, and an LED was turned on. Kuang et al. fabricated highly stretchable, self-healing SMP structures using UV-assisted DIW [30] (Figure 4D). Semi-interpenetrating polymer network elastomers containing shape-memory polyurethane were used. With the assistance of the shape-memory effect, a relatively large cracked surface was healed at an elevated temperature via entangled polymer chains.

Many 4D-printing studies have been conducted on the swelling feature of hydrogels. For example, Raviv et al. printed shape-changing 2D sheets consisting of a rigid plastic material and a water-swellable material [44]. Those materials were combined into a bilayer hinge and, when immersed in water, the overall structure was bent. The water-swellable material consisted of vinyl caprolactam, polyethylene, epoxy diacrylate oligomer, and curing agents. When immersed in water, the swellable material formed a hydrogel. Using similar materials, including hydroxyethyl acrylate, hydroxyethyl methacrylate (HEMA), and potassium 3-sulfopropylmethacrylate, Huang et al. demonstrated 3D-printed, programmable hydrogel structures [31] (Figure 4E). By illuminating certain patterns with different exposure times, they tuned the immersed state of structure. Another widely used hydrogel material is poly(N-isopropylacrylamide) (pNIPAM) [45, 46], which exhibits a temperature-dependent water swelling characteristic. It loses some water above the critical temperature, although it normally swells in water. Naficy et al. fabricated reversible shape-morphing structures using a printed bilayer structure of pNIPAM and pHEMA [47]. When the structure was immersed in water at 20°C, the swelling ratio of the pNIPAM was larger than that of the pHEMA, and the laminated structure was bent toward the pHEMA face. However, when the temperature increased to 60°C, the pNIPAM was dehydrated, and the swelling ratios of the two materials were reversed. Therefore, the bilayer was bent to the pNIPAM face. Additionally, biomimetic 4D printing was demonstrated using hydrogels that contained cellulose fibrils [48]. The local orientations of the fibrils were controlled during the printing to generate different swelling ratios in different parts, which led to various 3D shape changes.

LCEs have two states; nematic and isotropic states. At low temperatures, LCE molecules arrange into a linear shape. Above the transition temperature, the arrangement of the molecules breaks down, and LCEs transform into the isotropic, randomly organized state. Consequently, the overall size of the structure decreases. For example, thermo-responsive 4D printing has been conducted using LCEs. The typical materials used include 1,4-bis-[4-(3-acryloyloxypropyloxy) benzoyloxy]-2-methylbenzene (RM257) and 1,4-bis-[4-(6-acryloyloxhexyloxy) benzoyloxy]-2-methylbenzene (RM82). Yuan et al. fabricated a sequential folding box combining silver ink printing and elastomer/LCE printing and realized a laminated actuator structure [49]. With an applied electric bias, the temperature of the laminated actuator increased, because of Joule heating of the silver ink pattern. The ordinary elastomer material did not exhibit a significant change in length, whereas the LCE exhibited a significant decrease in length. Therefore, the laminated structure was bent to the LCE surface. Saed et al. fabricated another elastomer actuator using RM257 and RM82 [32] (Figure 4F). They molecularly engineered LCEs with two different monomers, different spacer polymers, and crosslinkers. The modulus, transition temperature, and viscosity of the LCEs were tuned. With different transition-temperature conditions, an actuator holding three different shapes in different temperature regimes was demonstrated. Ambulo et al. controlled the molecular direction of LCEs by controlling the DIW path [50]. With programming of the printing path, a printed flat structure morphed into a 3D structure when heated. Kotikian et al. 3D-printed RM82 LCEs using DIW at a high operating temperature [51]. By optimizing the printing speed and temperature, an LCE actuator was demonstrated. Above the transition temperature, the transition temperature, the length of LCE actuator decreased by 40% along the organized axis. This transformation was reversible over 100 cycles of

temperature variation. Additionally, programmable shape-morphing structures that transform from 2D to 3D or from one 3D structure to another 3D structure have been demonstrated by controlling the printing path. López-Valdeolivas et al. also fabricated a thermo-responsive lens for adaptive optics combining RM82 with optically transparent polydimethylsiloxane [33] (Figure 4G).

3 3D and 4D printing design and application for optics and metaphotonics

3.1 3D printing for optical and optoelectronic components

3D printing can be ideal for customized, complex optical components. For example, opto-mechanical components [52], photonic crystal fibers and waveguides [53], gratings, and lenses [54, 55] have been fabricated. 3D printing has special advantages for fabricating advanced optical components that are difficult to realize using conventional methods. Several optical elements can be fabricated and integrated together without an additional assembling process. Moreover, various freeform optical components can be realized, [56–60] because freeform optics often requires complex geometries that cannot be achieved with conventional symmetric shapes, 3D printing of freeform integrated optical components is attracting increasing attention in a variety of optical fields [61, 62]. For example, it could be important for lightweight, head-mounted displays for virtual reality and augmented reality [63, 64].

SLA—one of the common 3D printing methods—was invented by C. Hull in 1986 [65]. In SLA, a focused UV laser beam is applied to liquid photopolymers that are composed of monomers and oligomers and photo-initiators triggering polymerization [66–70]. After one layer is solidified by the laser beam, the same process is repeated for the subsequent layers. Recently, a parabolic mirror with nanometer-scale surface roughness (approximately 3 nm) was fabricated using SLA (Figure 5A) [71]. Its focused beam profile was almost identical to the beam from a mirror fabricated via conventional diamond milling [77]. Optical parts were printed using SLA and a wax printer then, a polymer mixture gel composed of methacrylates, acrylates, and urethane-based polymers was coated and UV-cured. The SLA 3D printing of transparent fused silica glass components at resolutions of a few tens of micrometers was also demonstrated recently [78]. The printed fused silica glass had the optical transparency of commercial fused silica glass and also had a smooth surface with a roughness of a few nanometers. Additionally, 3D printing of an optically clear ballistic gel has been considered for soft and stretchable optical components [79]. Although a smooth surface with a roughness of a few nanometers was achieved, it is still difficult to construct a nanometer-scale unit voxel using SLA.

DLW based on multi-photon absorption polymerization makes it possible to obtain a higher resolution [80]. High-power femtosecond laser pulses can increase the nonlinear multi-photon (usually two-photon) absorption and trigger the solidification of a small focal volume. Negative photoresists are typically used, and the parts exposed to laser remain after development. Many optical devices have been demonstrated using DLW, including waveguides [81], objective lenses [82], axicons [83], and optical sensors [84]. S. Maruo and S. Kawata applied two-photon absorption polymerization to the fabrication of a microscale structure for the first time [85]. A femtosecond laser beam was focused onto a photosensitive polymer, and crosslinking in the polymer occurred in the region of laser spot, because crosslinking occurs when the exposed dose of the beam exceeds polymerization threshold, only the very center of focused beam can overcome the polymerization threshold. This leads to polymerization in a subwavelength region. By scanning the laser focusing spot, it was possible to fabricate arbitrary 3D structures on the subwavelength scale [74, 86]. More recently, Gissibl et al. demonstrated sub-micrometer optical elements printed onto a single-mode fiber (Figure 5B) [72]. Optical elements such as spherical lenses, toric lenses, and freeform lenses with donut-shaped and top-hat-shaped intensity distributions were also demonstrated. The same group demonstrated ultracompact compound multi-lens objectives with micro- and nano-optical elements [87]. Furthermore, Thiele et al. directly printed a freeform lens on a complementary metal–oxide semiconductor image-sensor chip [73]. Four doublet objectives with different focal lengths and a common focal plane were printed together, with a footprint smaller than 300 μm × 300 μm. A foveated imaging system with a field-of-view (FOV) up to 70° was achieved (Figure 5C). When lenses with FOVs of 20°, 40°, 60°, and 70° were combined, the foveated image appeared even clearer.

3D printing has been also used to fabricate optical waveguides and optoelectronic devices. Using a stretched solution meniscus, Pyo et al. performed 3D printing of polystyrene nanowaveguides as well as a multiplexer and a splitter directly attached to a

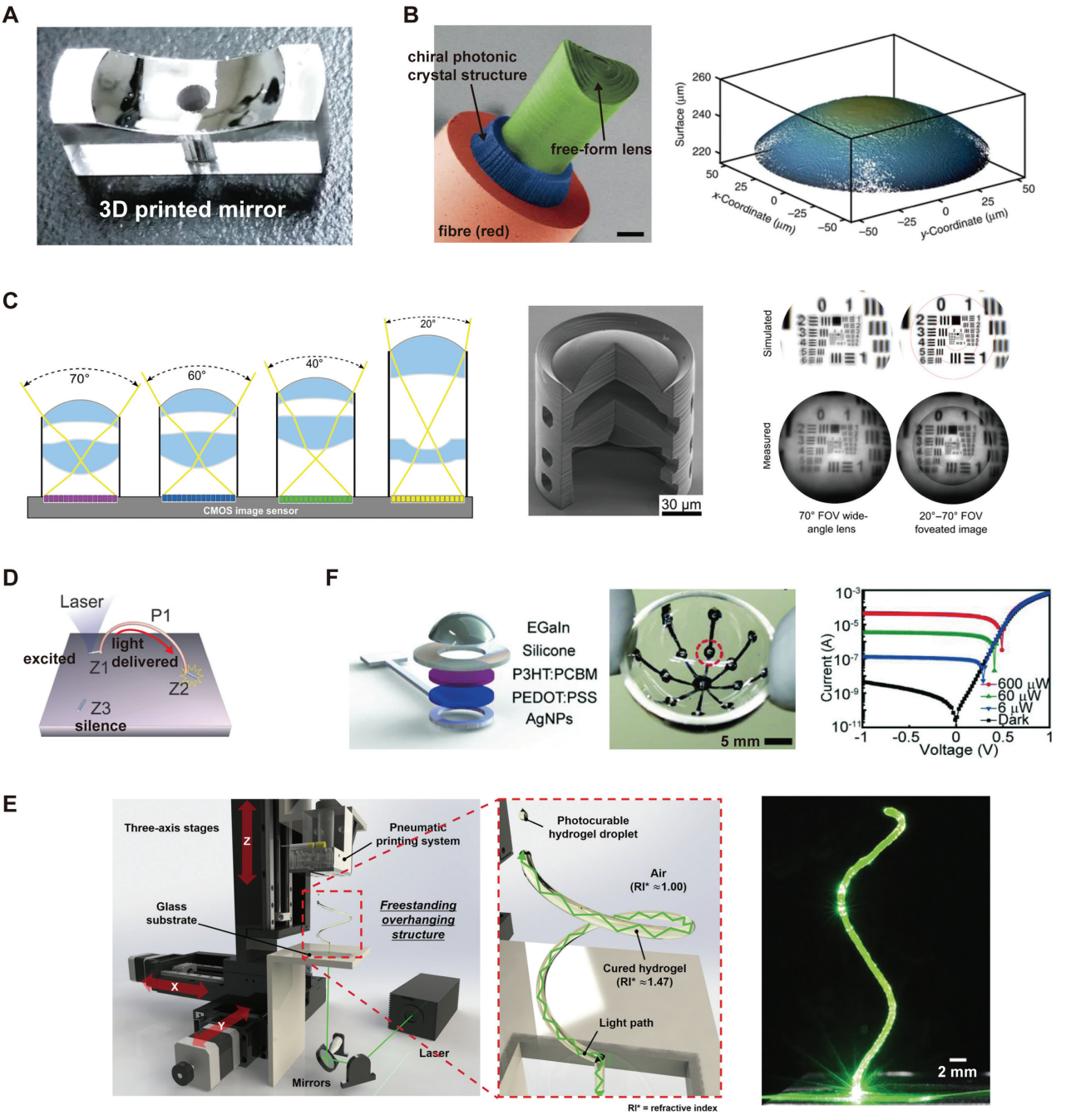

Figure 5: 3D printing for optical and optoelectronic components.
(A) 3D-printed parabolic mirror after smoothing and aluminum deposition. Adapted from Ref. [71]. Copyright (2018) Nature Publishing Group. (B) Left: Scanning electron microscope (SEM) image of a sub-micrometer optical element printed onto a single-mode fiber (scale bars: 25 μm). Right: Measured topography using optical interferometry of a spherical lens with a lens thickness of 250 μm, a radius of curvature 85.77 μm. Adapted from Ref. [72]. Copyright (2016) Nature Publishing Group. (C) Left: Four different FOV compound lenses on the same CMOS image sensor and the SEM image of a 3D-printed doublet lens. Right: Comparison of simulation and measurement images through a single compound lens with FOV of only a 70° (left), and with 20°, 40°, 60°, 70° (right). Adapted from Ref. [73]. Copyright (2017) AAAS. (D) Illustration explaining optical interconnection between two ZnO nanorods (Z1, Z2) through a polystyrene nanowire (P1). Adapted from Ref. [88]. Copyright (2016) John Wiley & Sons. (E) Left: Schematic view of the 3D printing system. The zoom-in part represents a 3D-printing method inspired by the light guide of an optical fiber. Right: Helical structure where light is guided and transmitted. Adapted from Ref. [75]. Copyright (2019) John Wiley & Sons. (F) Left: Schematic of the structure of the photodetector. Center: Photograph of the concentric photodetector array printed onto the inner surface of a hemispherical glass dome. Right: I-V characteristics of the photodetector onto the hemispherical glass dome. Adapted from Ref. [76]. Copyright (2018) John Wiley & Sons.

nanophotonic source [88]. When a ZnO nanorod (Z1) was excited by laser, its photoluminescence was successfully delivered to another nanorod (Z2) through the nanowaveguide (P1) (Figure 5D). They also fabricated an optical interconnect that delivered optical power over a gap (or a step) and functioned even under stretching. Lim et al. used photocurable hydrogels not only as a waveguide, but also as a source path simultaneously (Figure 5E) [75]. Light transmitted through the printed waveguide was used to polymerize the next droplet of the hydrogel precursor. This new 3D printing method employed the total internal reflection at the core (hydrogel)–cladding (air) interface. Smooth surfaces were printed without supports, and various freestanding overhanging and helical 3D structures were realized. Figure 5F shows polymer photodetectors 3D-printed via solution extrusion [76]. A photodetector was printed layer-by-layer, and the printed device was as smooth as spin-coated ones. The printed device exhibited an external quantum efficiency of 25.3% at –1 V and a rectification ratio of ~10^5 (ratio of forward to reverse diode current in the dark at ±1 V), which are comparable to those of microfabricated organic photodetectors. Photodetectors were also printed onto a curved surface (inner surface of hemisphere glass) and exhibited no deterioration in photodetection due to bending.

3.2 3D printing for optical metamaterials

DLW based on two-photon absorption polymerization can allow a patterning resolution of <100 nm and has been used to fabricate various nanophotonic structures and optical metamaterials, such as log-pile photonic crystals [89], spiral photonic crystals, and 3D split-ring metamaterials [90]. Figure 6A and B show periodically arranged standing U-shaped resonators (SUSRs) that exhibit perfect absorption or reflection depending on the incidence polarization [91]. After two-photon absorption polymerization patterning, gold-layer coating via magnetic sputtering was performed. The fabricated 3D SUSRs exhibited perfect absorption for *x*-polarized light. Additionally, they exhibited perfect reflection for *y*-polarization. Figure 6C and D show the simulated and measured spectra. 94% absorption was experimentally achieved at the mid-infrared (IR) frequency of 1200 cm^{-1}. The fabricated structure also exhibited sufficient thermal stability, even though it was composed of polymer materials. There was no significant change of the resonant absorption peak up to 100°C. At 200°C, the gold layer on top of the photoresist began to soften, and the absorption value decreased slightly to 92%. However, above 350°C, the overall SUSR structure began to collapse.

As another example, DLW was used to fabricate a 3D carpet invisibility cloak operating in the near-IR range [93]. By exploiting transformation optics (TO), a gradual variation of the refractive index in a woodpile structure was realized by varying the fill factor. The same group reduced the feature size of the patterned polymer by incorporating an additional depletion laser together with a two-photon absorption exciting laser. In this way, they reduced the spacing between beams in the woodpile structure from 800 to 350 nm and realized a polarization-independent 3D carpet invisibility cloak in the visible range [92]. The structure in the upper part of Figure 6E is a reference that does not provide cloaking, whereas that in the lower part provides cloaking. The blue part is the woodpile of the polymer structure, and the yellow indicates the sputtered 100-nm-thick gold film. Figure 6F shows a microscope image of the cloaking structure. When inspected from the glass-substrate side, the reference sample exhibited dark stripes. However, it was impossible to observe dark stripes in the cloaking structure. Cloaking occurred for wavelengths larger than ~700 nm, and it persisted up to a longer wavelength (3 μm) as long as the woodpile polymer remained transparent. The measurement results were well explained by ray-tracing simulations.

3.3 3D printing for terahertz components

The resolution of common 3D printing methods (such as FDM and PolyJet) can reach a few tens of micrometers thus, THz components can be fabricated using 3D printing [94]. For example, Gospodaric et al. fabricated dielectric phase plates for THz beam shaping (Figure 7A and B) [95]. Proper phase modulation profiles were calculated using the Gerchberg–Saxton iterative algorithm, and a Gaussian beam was transformed into arbitrary images via the phase plates. Polylactic acid (PLA) was printed with proper coordinates and proper thicknesses to realize the required phase modulation. Additionally, a THz polarizer was fabricated using commercial conductive PLA filaments, where carbon black was mixed in a PLA matrix (Figure 7C and D) [96]. The THz polarizer was 3 cm in diameter and consisted of 0.3-mm-wide stripes that were separated by 0.3-mm air gaps (fill factor 50%). The response of the printed THz polarizer was investigated via simulations and measurements. At 0.3 THz, TM-polarized waves could pass through the printed polarizer, while TE-polarized waves were attenuated strongly at a distance no longer than 2 mm. However, this polarization response

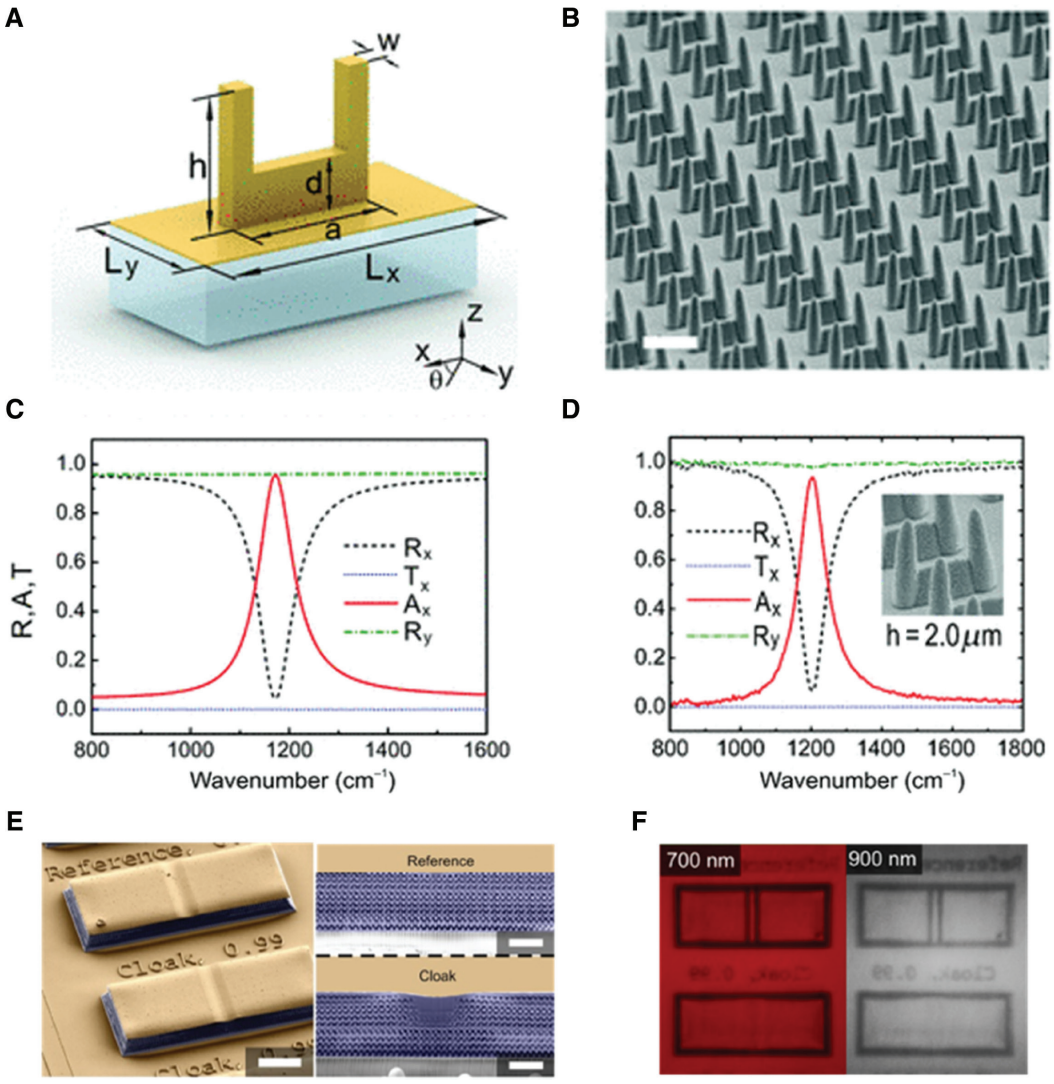

Figure 6: 3D printing for optical metamaterial.
(A) Schematic of the standing U-shape resonator with $L_x = 4$ μm, $L_y = 2$ μm, a = 2 μm, h = 2 μm, d = 0.7 μm, and w = 0.3 μm. (B) FESEM micrographs of the SUSRs with h = 2 μm (scale bar: 2 μm). (C) Simulation result of the SUSRs with the same parameter of Figure 3B. (D) Measured spectra of the SUSRs with h = 2 μm. Adapted from Ref. [91]. Copyright (2013) APS. (E) SEM images of reference and cloak samples. The blue color indicates polymers and the yellow one indicates a sputtered gold film (scale bar, 10 μm). (F) Measured images of reference (top) and cloak (bottom) samples at different wavelengths. Adapted from Ref. [92]. Copyright (2011) OSA Publishing.

was reversed at higher frequencies above 0.5 THz. As shown in Figure 7D, TE-polarized waves passed through the structure at 2.5 THz, but TM-polarized waves were attenuated.

3.4 3D printing for microwave metamaterials and transformation optics

3D printing is advantageous for metamaterial fabrication, because metamaterials often require sophisticated structures that are difficult to fabricate via traditional methods. In particular, 3D printing is suitable for microwave metamaterials, where the wavelengths are on the order of centimeters. There have been various studies on dielectric metamaterials and TO, because dielectric materials are commonly used in 3D printing. For example, polycarbonate (with a dielectric constant of 2.57) was used to manufacture uniaxial anisotropic metamaterials via FDM 3D printing [97]. Polymer composites that include microsized ceramic powders in a polymer matrix have also been investigated for achieving a high permittivity. Figure 8A shows two 3D diamond-like lattices with low (right) and high (left) permittivity values [98]. While the low-permittivity lattice contains only ABS, the high-permittivity one consists of ABS and $BaTiO_3$

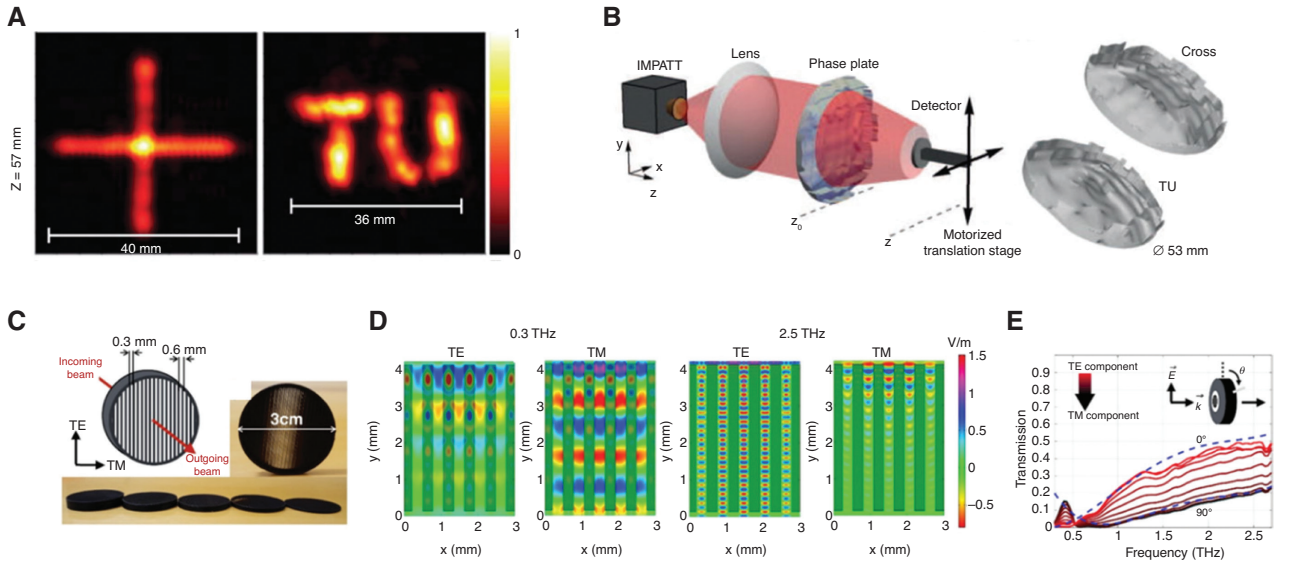

Figure 7: 3D printing for THz applications.
(A) Measured intensity profiles of a cross and a university logo of the optical field by an incidence of THz wave. (B) Schematic of the optical setup for intensity profile measurements. Adapted from Ref. [95]. Copyright (2018) AIP publishing. (C) Photograph of a 3D-printed polarizer. (D) Numerical simulation results for the 4 mm propagation length. Light is incident along the y-axis (from the top). The dark green region is a conductive PLA part, while the light green region is air. (E) Transmission amplitude of the THz beam measured after passing through 4 mm polarizer. The dashed lines are numerical predictions for the TE and TM mode. Adapted from Ref. [96]. Copyright (2019) OSA Publishing.

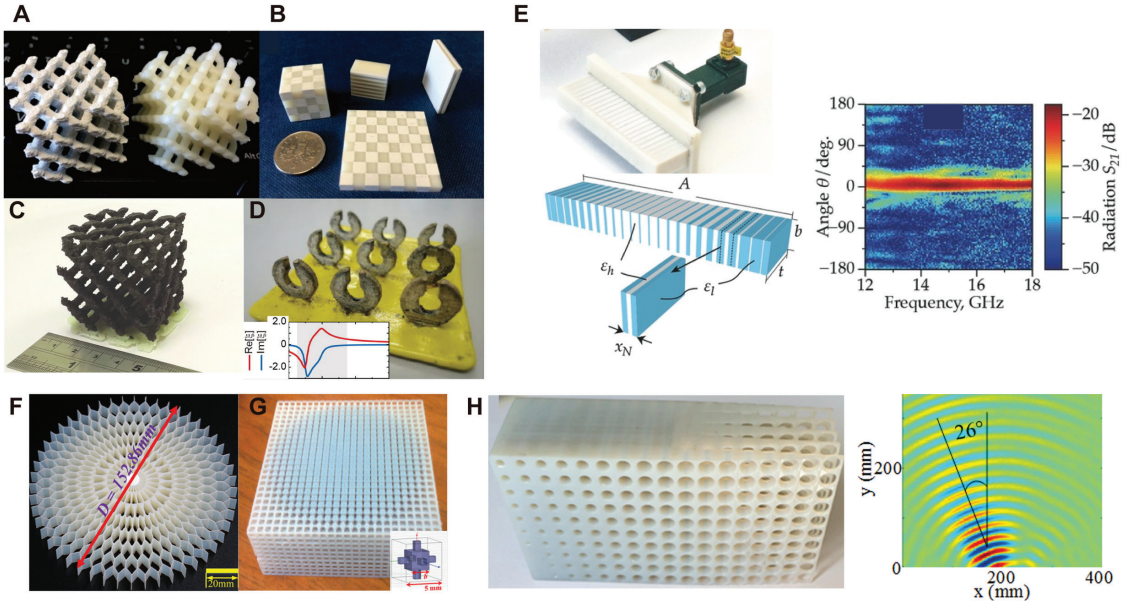

Figure 8: 3D printing for microwave metamaterials and transformation optics.
(A) Diamond-like lattice composed of ABS only (right) and ABS + $BaTiO_3$ composite (left). (B) Samples composed of alternating areas of ABS and ABS + $BaTiO_3$ that are printed using a dual-extrusion nozzle. (C) Diamond-like lattice made of ABS with a 10 vol% NiZn ferrite filament. Adapted from Ref. [98]. Copyright (2015) The Royal Society Publishing. (D) PLA-SRRs sample after selective electroless plating on an ABS structure (inset: anti-resonant dispersion for bi-anisotropy). Adapted from Ref. [99]. Copyright (2017) AIP Publishing. (E) Left: Schematic of a GRIN lens with low (blue) and high (white) relative permittivity regions and photograph of the short horn with 3D-printed GRIN lens. Right: Experimental radiation pattern of the GRIN lens. Adapted from Ref. [100]. Copyright (2016) John Wiley & Sons (F) Photograph of a 3D-printed planar Luneberg lens. Adapted from Ref. [101]. Copyright (2018) ACS Publications. (G) 3D-printed Luneburg lens antenna (inset: schematic of the cubic-unit cell). Adapted from Ref. [102]. Copyright (2014) IEEE. (H) Photograph of a 3D-printed beam steering lens and the measured electric field distribution for the lens antenna. Adapted from Ref. [103]. Copyright (2016) IOP Publishing.

microparticles, and its dielectric constant was increased to 8.72 at 14 GHz for 70 wt% $BaTiO_3$ [104]. Complex geometries and the desired spatial distribution of the dielectric properties can be achieved using a dual-nozzle printing head. Figure 8B presents an example; the alternating low- and high-permittivity areas consist of ABS and ABS/$BaTiO_3$ composites, respectively. As shown, layered slabs, cubes, and even checkerboard structures were well demonstrated, with clear boundaries and alignments. A one-dimensional (1D) layered slab comprising alternating photonic structures was experimentally confirmed to have anisotropic dielectric permittivity and support Mie-type resonances in the microwave frequency range [105].

Mixing of different materials can result in diverse material properties. Figure 8C shows the same diamond-like lattice as Figure 8A, but it is made of ABS/NiZn ferrite composites [98, 106]. However, compared with pure dielectric composites, magnetic composites with a high permeability have attracted less research attention, as magnetic particles tend to agglomerate, and their electric and magnetic responses are reduced. In contrast, highly conductive filaments consisting of metal particles and polymers have already entered the commercial market for desktop 3D printers; for example, such a conductive filament allowed the design of a microwave metamaterial with a high permittivity of 14 at approximately 1 GHz [107]. On the other hand, 3D-printed dielectric structures were also used as templates for surface metallization [99, 108, 109]. Because vacuum evaporation and sputtering often encounter difficulties for full metallization onto highly complex 3D structures, a wet chemical process is advantageous for obtaining a uniform coating without shaded areas. For example, selective electroless plating was used to demonstrate self-standing split-ring resonators that exhibited a bi-anisotropic response (Figure 8D).

Dual-extrusion 3D printers can readily allow alternating variations in permittivity, which are often required for TO. The left panel of Figure 8E presents a gradient refractive index (GRIN) lens composed of sub-elements with varied effective local permittivity values [100]. The blue region corresponds to a relatively low permittivity ε_l (made of ABS), and the white corresponds to a high permittivity ε_h (made of ABS/$SrTiO_3$ composites). The effective local permittivity ε_N of the sub-elements consisting of blue and white layers can be determined as $\varepsilon_N = f\varepsilon_h + (1-f)\varepsilon_l$, where f represents the relative volume fraction of the high-permittivity component. In the proposed GRIN lens, f decreased toward the end of the structure; consequently, ε_N also decreased. The 3D-printed GRIN lens produced a significantly directed far-field radiation pattern at an operating frequency range centered at 15 GHz [right panel of Figure 8E]. The fabrication of GRIN lenses can be achieved not only with an alternating permittivity, but also with a single dielectric material that includes voids of graded sizes. In this case, the permittivity of the voids corresponds to $\varepsilon_l = 1$. The honeycomb structure shown in Figure 8F is one example [101]. It was fabricated via SLA and allowed a gradual change of ε_N. The photocurable resin circular lens was divided into 10 concentric rings and patterned with inverse Y-shaped structures. Another example is shown in Figure 8G; an elaborate 3D Luneburg lens was realized by varying the fill factor gradually from the center to the surface of the lens [102]. Accordingly, a gradual decrease in ε_N was achieved. Another example of 3D-printed TO components is the beam-steering lens shown in Figure 8H [103]. An all-dielectric microwave lens was fabricated via PolyJet 3D printing and included circular voids that increased in size toward the upper-right region. This structure allowed beam steering over a broad frequency range without resonance. Beam steering with an angle of 26° was demonstrated at 12 GHz.

3.5 Inverse-designed metastructures at microwave and optical frequencies

Inverse design is one of the computational methods for identifying the optimal geometry to obtain the desired output. Inverse design involves iterative calculations with given parameters, eventually arriving at the desired objective. Owing to its fast and automatic calculations, the inverse-design method has been used in optics to overcome the shortcomings of conventional methods and is gaining popularity [110–117]. 3D printing can be an ideal solution for device fabrication as inverse design often requires complex geometries (or a complex permittivity distribution). Recently, Estakhri et al. suggested an inverse-designed metaphotonic platform (Figure 9A) to solve the general Fredholm integral equation of the second kind in an analog manner for wave propagation in metastructures [118]. Any arbitrary monochromatic wave $g(u)$ is transferred to a metamaterial represented by a given integral operator with kernel $K(u, v)$. The output of the operator is conveyed to the input side, and then the system obeys the source-free equation $g(u) = \int_a^b K(u, v)g(v)dv$. Next, the input signal $I_{in}(u)$ is inserted into the integral equation by exploiting a set of coupling elements along the waveguide, and many iterations of this process eventually approach the intended result. An experimental verification was performed at a

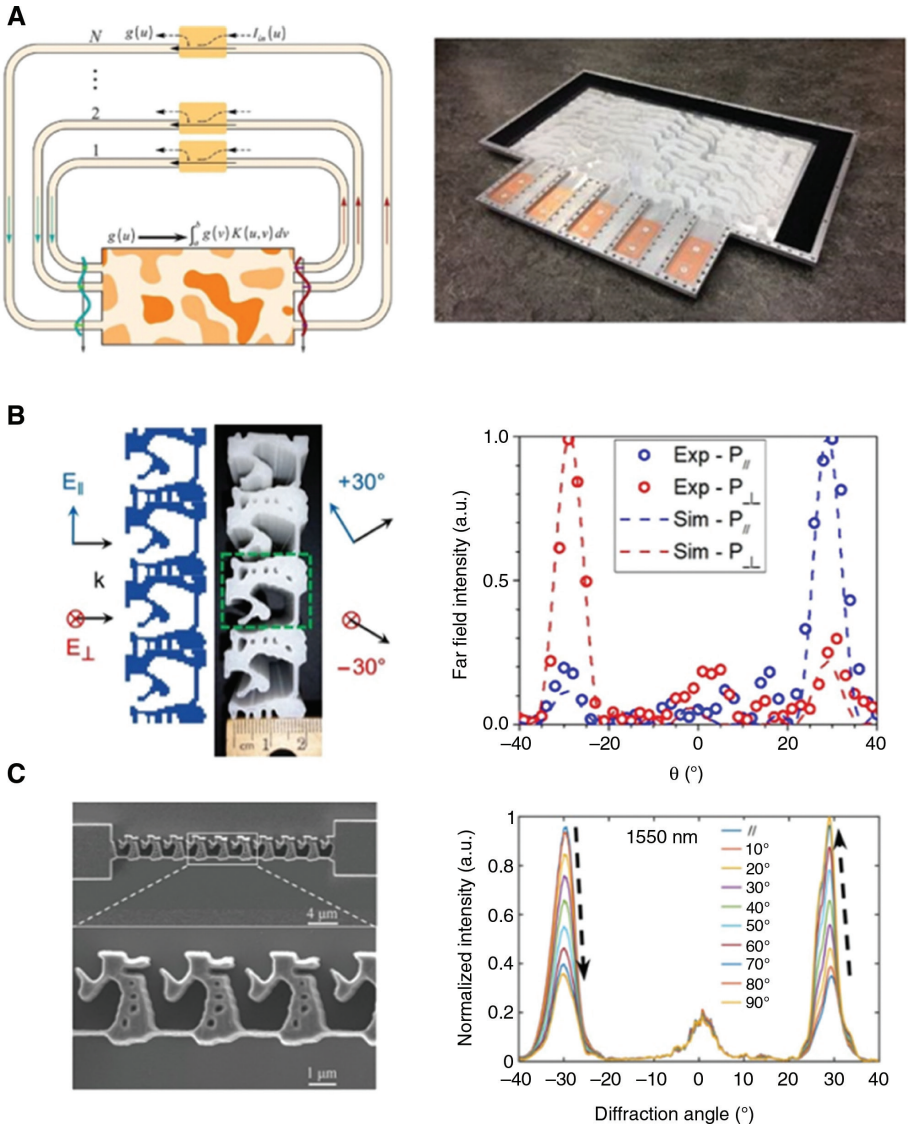

Figure 9: Inverse-designed metastructures.
(A) Left: Sketch of a closed-loop network, consisting of a suitably designed kernel operator (metamaterial block), feedback mechanism, and in/out coupling elements to excite and probe the waves. The N waveguides realize the external feedback network. The direction of the wave flow is indicated by arrows. Right: Photograph of the constructed metamaterial. Adapted from Ref. [118]. Copyright (2019) AAAS. (B) Left: Schematic drawing and top-view photograph of the 3D-printed inverse-designed 30° polarization splitter. With parallel(vertical) electric-field polarization $E_{\parallel}(E_{\perp})$, the input plane wave is bent to +30° (−30°). Right: Simulated (dashed line) and measured (circles) far-field power profiles for both parallel and perpendicular polarizations. Adapted from Ref. [119]. Copyright (2018) Nature Publishing Group. (C) Left: Scanning electron micrograph of the top view of the printed device. Right: Normalized experimental transmitted intensity of the fabricated sample as a function of diffraction angle for various input polarization angles. Adapted from Ref. [120]. Copyright (2019) John Wiley & Sons.

microwave frequency using a 3D-printed metastructure (see the right panel in Figure 9A).

Callewaert et al. demonstrated a broadband, polarization-dependent beam splitter based on inverse-designed non-resonant structures [119]. An optimized binary structure was obtained via inverse design, and the polystyrene/air binary structure was fabricated via FDM 3D printing (Figure 9B). The inverse-designed beam splitter had several merits: high transmission efficiency (>60%), broadband response ($\Delta\lambda/\lambda > 25\%$), and the use of a dielectric-based thin structure ($\leq 2\lambda$). The beam splitter worked at approximately 30 GHz and was a few centimeters in size. More recently, the same group extended this beam-splitter design to the near-IR range [120]. An inverse-designed polarization beam splitter was realized via DLW (Figure 9C). It exhibited diffraction angles of ~25° at 1.3 μm and ~30° at 1.55 μm in experiments, which agreed well with simulations.

3.6 4D printing of photoresponsive materials for active optical structures

Compared with other external stimuli (such as heat, moisture, and pH), light has unique advantages; it can enable structural changes remotely and can also enable local control with a high resolution in space and time. Various properties of light (intensity, polarization, wavelength, etc.) can be rapidly and precisely adjusted to control the material response. Therefore, 4D printing of photoresponsive materials is promising for the fabrication of various optical structures [121–124]. Among the photoresponsive materials, azobenzene is the most widely studied. The isomerization state of azobenzene compounds transforms from trans to cis under illumination at certain wavelengths (mostly in the UV region) [125]. For example, azobenzene compounds were mixed with photopolymer liquid resins for SLA and used to fabricate a photoresponsive smart window (Figure 10A) [126]. The transmission spectra were measured with crossed polarizers. Without optical pumping, there was no transmission through the window. However, with pumping, optical anisotropy was induced, because of the trans–cis transformation of the azobenzene compounds. This led to the polarization rotation of the incident light, and the transmission through the window increased. After the pumping light was turned off, the azobenzene compounds transformed back into the trans state. Therefore, the transmission decreased. It was possible to modulate the transmitted beam with a frequency of 100 Hz (Figure 10B).

Additionally, azobenzene compounds can be combined with linearly oriented liquid crystals that have birefringence along the ordinary and extraordinary axes [128–131]. For example, Nocentini et al. fabricated photoresponsive 3D photonic circuits with azobenzene compounds in liquid crystals [127]. DLW was used to fabricate an optical waveguide operating at approximately 1550 nm. Furthermore, a waveguide-coupled ring resonator was patterned to excite resonant optical modes (Figure 10C). To introduce photoresponsivity, an additional cylindrical structure made of azo-compound-doped liquid crystals was added to the ring resonator. Under green laser illumination, the resonance wavelength was redshifted, because of the change in the resonator size. In a modified structure, the refractive-index variation of the liquid crystals was induced, which led to the blueshift of the resonance. The resonance shift was affected by the laser power. As the illuminating power of the laser increased, the resonance shift increased. Other stimuli, such as temperature and pH changes, have also been employed to actively control photonic devices [132–134].

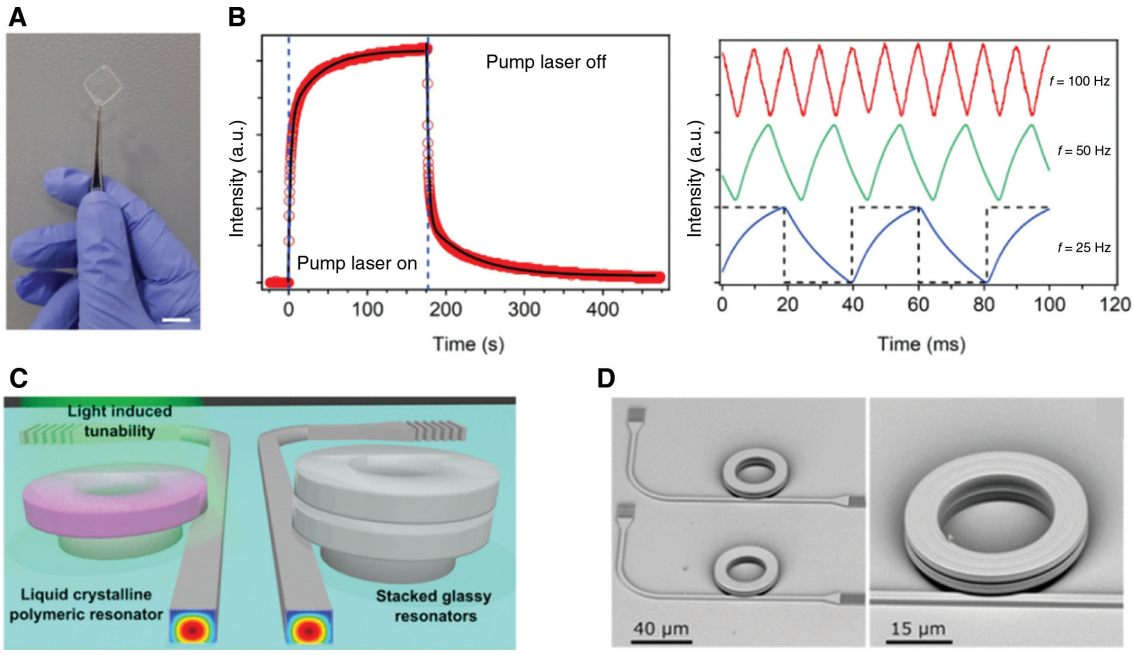

Figure 10: 4D printing of photoresponsive materials.
(A) Photograph of an optical window after polishing (scale bar: 1 mm). (B) The intensity value with the 532 nm pump laser on and off states. There is an abrupt intensity growth with the pump laser on and a decay of the intensity without the pump laser. The modulation of the transmitted beam was demonstrated up to 100 Hz. Adapted from Ref. [126]. Copyright (2019) SPIE. (C) A schematic of the light-tunable whispering gallery mode resonator. The pink color indicates the liquid crystal polymer region. (D) SEM images of the fabricated waveguide with whispering gallery mode resonators. Adapted from Ref. [127]. Copyright (2018) ACS Publications.

3.7 4D printing for stimuli-responsive microwave structures

4D printing combines smart materials with 3D printing and can thus realize smart materials with a complex geometry and fine details. Therefore, it is promising for the fabrication of various stimuli-responsive structures with highly enhanced functionalities. Recently, microwave Fano-resonant structures that exhibited sharp spectral resonances were demonstrated via 4D printing of SMPs [135]. The typical spatial resolution in 3D printing can reach tens of micrometers. Therefore, 4D printing is suitable for the fabrication of microwave active structures. Figure 11 shows the general idea. An SMP beam array was fabricated via FDM printing. After thermomechanical programming, the SMP lattice was randomized. This disordered lattice does not exhibit a sharp spectral resonance, whereas the ordered lattice can exhibit sharp Fano resonances. When heated above the glass-transition temperature, disordered lattices are transformed into an ordered lattice, significantly changing the microwave spectrum. This stimuli-responsive action occurs as a result of material properties and thus does not require an electric power supply. Thus, it can be used for creative applications, such as long-distance environmental monitoring via microwave detection. With various smart materials, 4D printing might provide a unique platform for active, reconfigurable microwave structures.

In experiments, PLA was used as the SMP. PLA is a thermoplastic material that is suitable for FDM printing and has a clear shape-memory property. Figure 12A shows two pictures of the lattice sample used in experiments before and after heating. The deformed lattice recovered to the original, ordered lattice upon heating. To characterize the spectral response of the lattice structures precisely, three identical samples were prepared with different randomness (Figure 12B). Figure 12C shows the measured transmission spectra of these three lattices for transverse-electric (TE) polarization. The disordered lattice with large randomness exhibited essentially no resonance (blue curve), whereas that with smaller randomness exhibited a very broad resonance at 38–40 GHz. In the ordered lattice, a sharp Fano resonance was observed at approximately 36.7 and 39.1 GHz. Figure 12D compares the experimental and simulated transmission spectra for the ordered lattice in the cases of TE and transverse-magnetic (TM) polarization. Although both polarizations resulted in Fano resonances, the TM-polarization resonance was broader than the TE-polarized one. The effect of the degree of disorder on the Fano resonance was investigated using numerical simulations. Figure 13 shows how the Fano resonance spectrum and the field profile changed as the degree of disorder increased. As the degree of disorder increased, the sharp Fano resonance was blue-shifted, and the resonance was broadened and weakened. Additionally, the field profile of the guided resonance became

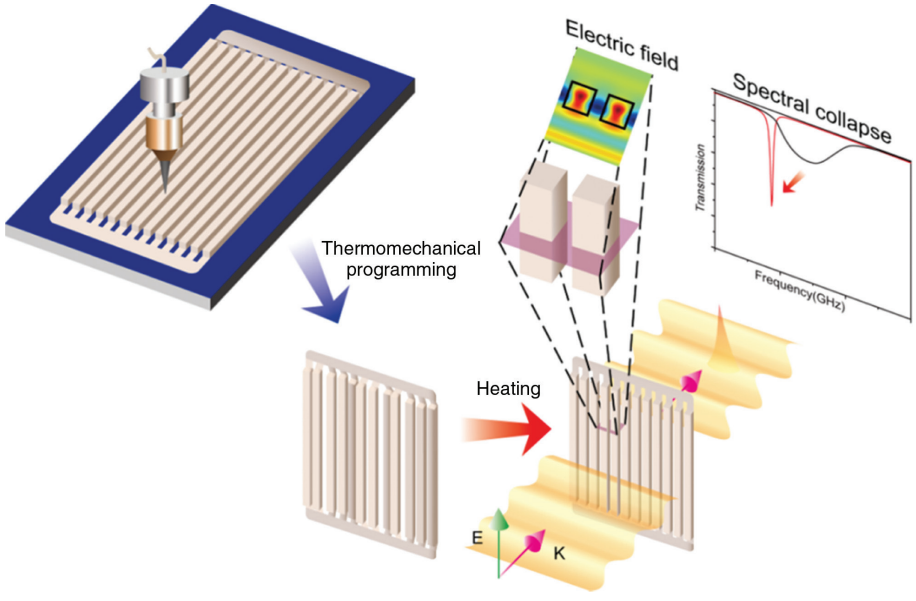

Figure 11: Schematic of a stimuli-responsive SMP photonic structure.
The 3D-printed SMP lattice is randomized into a disordered one. The disordered lattice does not exhibit a sharp spectral resonance. But, when heated above the glass transition temperature, the disordered lattice is transformed into an ordered lattice, exhibiting a sharp Fano resonance. Reprinted from Ref. [135]. Copyright (2019) John Wiley & Sons.

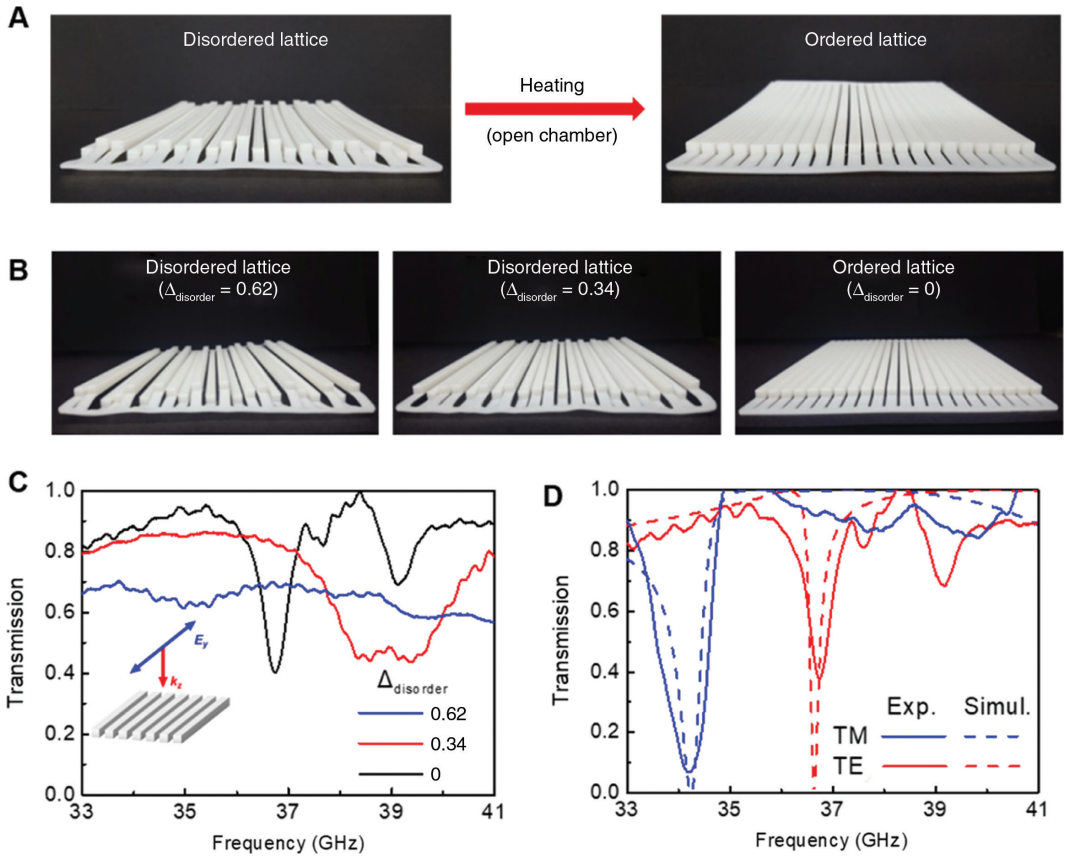

Figure 12: Spectra response of ordered and disordered lattices.
(A) Photographs of disordered and ordered SMP lattices. The disordered lattice returned to an ordered one in an open chamber (hot oven). (B) Photographs of SMP lattices with different degrees of disorder. The ordered lattice has $\Delta_{disorder} = 0$. (C) Transmission spectra for three samples in Figure 12B. (D) Comparison of measured and simulated spectra for TE- and TM-polarized transmission. Adapted from Ref. [135]. Copyright (2019) John Wiley & Sons.

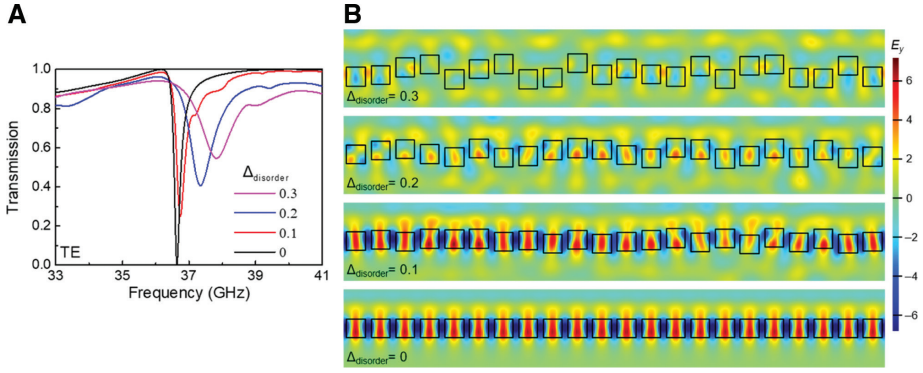

Figure 13: Simulation results.
(A) Simulation spectra for TE-polarized transmission with different degrees of disorder. (B) Simulated electric field profiles (E_y). The field profile of the guided resonance becomes more randomized as $\Delta_{disorder}$ increases. This behavior happens when the Fano resonance in the dielectric lattice structure is induced by a coherent mode distributed over the whole lattice, not by localized resonances in individual beams. Adapted from Ref. [135]. Copyright (2019) John Wiley & Sons.

more randomized. In the dielectric lattice structure, sharp Fano resonances occurred, because of guided resonances in the periodic, dielectric beams, which interfered with the slowly varying background Fabry–Perot resonance. Upon heating, a sharp spectral change occurred, because the Fano resonance in the ordered lattice structure was induced by a collective mode distributed over the whole lattice, not by localized resonances in individual beams.

4 Conclusions and perspectives

In this paper, we have introduced recent developments in 3D and 4D printing and covered topics that are of interest for the nanophotonics and metaphotonics communities. We first discussed functionalized inks and filaments embedded with nanoparticles or conductive materials and also discussed available materials for 4D printing. Then, we presented the various designs and applications of 3D printing in the optical, THz, and microwave domains. We also introduced the developments in 4D printing for active structures in the optical and microwave regimes.

Dielectric materials are commonly used in 3D printing and have been applied to various dielectric optical structures, but many metaphotonic designs can still benefit from highly conductive materials. In fact, metal 3D printing via SLS is being actively studied for optimizing mechanical parts and reducing their weight. Similar to other 3D printing methods, SLS metal printing has advantages for fabricating arbitrary shapes. Moreover, it is a bottom-up fabrication process, which is different from the conventional top-down fabrication method based on subtractive manufacturing from bulk materials. Thus, metal powders can be recycled in SLS, and the amount of material waste can be reduced. However, SLS metal 3D printing still have many issues that must be resolved before it can be applied to optical and metaphotonic structures. First, because of the layer-by-layer fabrication process, it suffers from significant surface roughness. The surface of the as-printed structures is too rough for application as optical components [136, 137]. Therefore, surface treatments such as grinding or polishing are required, complicating the fabrication procedure. Second, because of the melting or sintering of the powder, the printed structures have internal thermal stress. This internal stress can cause structural distortion over time. Therefore, annealing is often needed to remove thermal stress, further increasing the complexity of the fabrication procedure.

3D metal structures can be also created via metal ink printing. Recently, freestanding 3D metal structures were fabricated via local sintering of silver nanoparticle inks using an IR laser [138]. The IR laser can convert separated silver nanoparticles into aggregated ones with high conductivity. This IR laser sintering allows the patterning and annealing processes to be performed together in air. Figure 14A shows this process. The collimated laser was focused to a 100 μm point. Silver nanoparticles mixed in solvents were dispensed through a syringe using a pressure controller. When they were extruded in the substrate or air, the laser was focused on the silver inks, sintering them rapidly. By positioning or rotating the substrate, various 3D shapes were fabricated. Figure 14B and C show printed freestanding structures: a helical coil and a butterfly shape. 3D printing of such freestanding metal structures can allow greater freedom in the design of various metaphotonic structures.

New ideas and methods for 3D printing are being introduced to achieve large printing volumes with a high

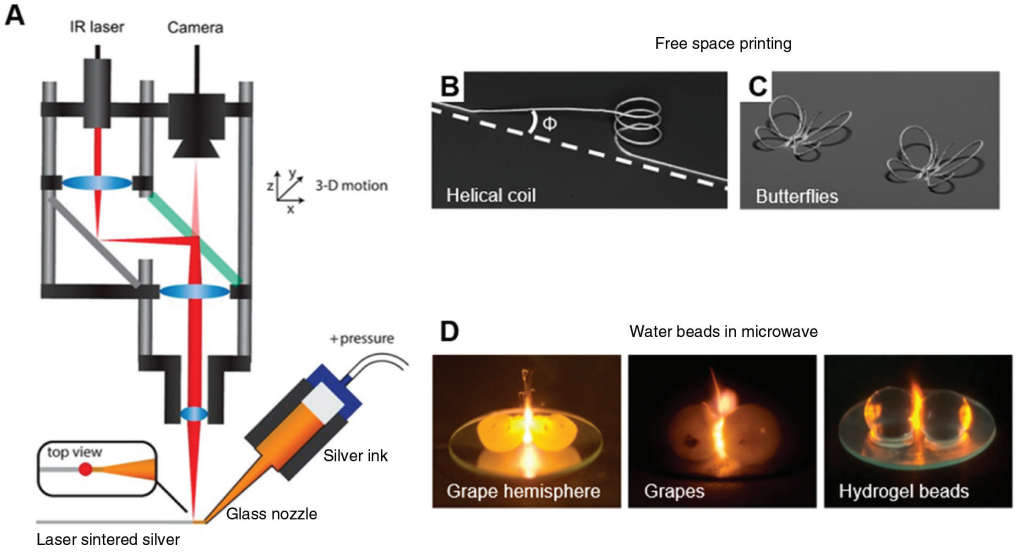

Figure 14: Future perspectives.
(A) Schematic for metal-ink 3D printing with IR laser sintering. (B) freestanding helical coils (diameter: 500 μm). (C) Printed butterflies with freestanding wings. Adapted from Ref. [138]. Copyright (2016) National Academy of Sciences. (D) Plasma is formed between two grape (or hydrogel) beads, because of strong microwave field enhancement in the gap. Adapted from Ref. [139]. Copyright (2019) National Academy of Sciences.

throughput [140, 141]. Additionally, more printing materials are becoming available. The rapid development of multi-material 3D printing technologies is introducing many new possibilities and opportunities for 4D printing. Either extrusion or jet-type 3D printing can be used for multi-material 3D printing; several filaments made of different materials can be employed together using multi-nozzle extrusion-type printers, or several inks for different materials can be dynamically mixed together in jet-type 3D printers. SLA or DLW can also allow multi-material 3D printing when the fabrication process is repeated with different materials. With various printable smart materials, 4D printing might provide a unique platform for active, reconfigurable optical and microwave structures. These active structures can introduce unprecedented opportunities in nanophotonics and metaphotonics and may have applications in active photonic devices, optical sensors, displays, and antennas. With biocompatible materials (such as hydrogels), implantable and stimuli-responsive photonic devices can be developed for biomedical applications. There are abundant new opportunities for investigation. For example, it was recently demonstrated that a dimer of aqueous beads induced strong field enhancement in the gap upon microwave incidence (Figure 14D) [139]. Hydrogels consist of mostly water (>99%) and are commonly used in 4D printing. Thus, there could be interesting research opportunities involving the combination of stimuli-responsive functions with the microwave response in 3D-printed hydrogel structures.

Our review can be helpful for researchers in the nanophotonics and metaphotonics communities who wish to learn about recent ideas and developments in 3D and 4D printing. We hope that our work stimulates further developments in this rapidly growing field.

Acknowledgements: We acknowledge financial support from the National Research Foundation (NRF) of Korea (NRF-2018R1E1A2A02086050, Funder Id: http://dx.doi.org/10.13039/501100003725, NRF-2019R1A2C1008330).

References

[1] Lipson H, Kurman M. Fabricated: the new world of 3D printing. Indianapolis, Indiana, USA: John Wiley and Sons, 2013.
[2] Gibson I, Rosen D, Stucker B. Additive manufacturing technologies: 3D printing, rapid prototyping, and direct digital manufacturing. Berlin, Germany: Springer, 2014.
[3] Jeong HY, An SC, Seo IC, et al. 3D printing of twisting and rotational bistable structures with tuning elements. Sci Rep 2019;9:324.
[4] Gu DD, Meiners W, Wissembach K, Poprawe M. Laser additive manufacturing of metallic components: materials, processes and mechanisms. Int Mater Rev 2012;57:133.
[5] Klippstein H, Sanchez ADDC, Hassanin H, Zweiri Y, Seneviratne L. Fused deposition modeling for unmanned aerial vehicles (UAVs): a review. Adv Eng Mater 2018;20:1700552.
[6] Waheed S, Cabot JM, Macdonald NP, et al. 3D printed microfluidic devices: enablers and barriers. Lab Chip 2016;16:1993.
[7] Au AK, Huynh W, Horowitz LF, Folch A. 3D-printed microfluidics. Angew Chem Int Ed 2016;55:3862–81.
[8] Melchels FPW, Domingos MAN, Klein TJ, Malda J, Bartolo PJ, Hutmacher DW. Additive manufacturing of tissues and organs. Prog Polym Sci 2012;37:1079–104.
[9] Gleadall A, Visscher D, Yang J, Thomas D, Segal J. Review of additive manufactured tissue engineering scaffolds: relationship between geometry and performance. Burns Trauma 2018;6:19.
[10] Awad A, Trenfield SJ, Gaisford S, Basit AW. 3D printed medicines: A new branch of digital healthcare. Int J Pharm 2018;548:586–96.
[11] Baev A, Prasad PN, Ågren H, Samoć M, Wegener M. Metaphotonics: an emerging field with opportunities and challenges. Phys Rep 2015;594:1–60.
[12] Tibbits S. The emergence of "4D printing". In: TED conference, 2013.
[13] Ge Q, Qi HJ, Dunn ML. Active materials by four-dimension printing. Appl Phys Lett 2013;103:131901.
[14] Tibbits S. 4D printing: multi-material shape change. Architectural Design 2014;84:116–21.
[15] Teoh JEM, Zhao Y, An J, Chua CK, Liu Y. Multi-stage responsive 4D printed smart structure through varying geometric thickness of shape memory polymer. Smart Mater Struct 2017;26:125001.
[16] Wu J, Yuan C, Ding Z, et al. Multi-shape active composites by 3D printing of digital shape memory polymers. Sci Rep 2016;6:24224.
[17] Jiang Y, Korpas LM, Raney JR. Bifurcation-based embodied logic and autonomous actuation. Nat Commun 2019;10:128.
[18] Jeong HY, Lee E, Ha S, Kim N, Jun YC. Multistable thermal actuators via multimaterial 4D Printing. Adv Mater Technol 2019;4:1800495.
[19] Duigou A Le, Chabaud G, Scarpa F, Castro M. Bioinspired electro-thermo-hygro reversible shape-changing materials by 4D printing. Adv Funct Mater 2019;29:1903280.
[20] Mao Y, Yu K, Isakov MS, Wu J, Dunn ML, Qi HJ. Sequential self-folding structures by 3D printed digital shape memory polymers. Sci Rep 2015;5:13616.
[21] Chen T, Bilal OR, Shea K, Daraio C. Harnessing bistability for directional propulsion of soft, untethered robots. Proc Natl Acad Sci USA 2018;115:5698–702.
[22] Haring AP, Khan AU, Liu G, Johnson BN. 3D printed functionally graded plasmonic constructs. Adv Opt Mater 2017;5:1700367.
[23] Kong YL, Tamargo IA, Kim H, et al. 3D printed quantum dot light-emitting diodes. Nano letters 2014;14:7017–23.
[24] Wang F, Chong Y, Wang F, He C. Photopolymer resins for luminescent three-dimensional printing. J Appl Polym Sci 2017;134:44988.
[25] Hotta M, Hayashi M, Lanagan MT, Agrawal DK, Nagata K. Complex permittivity of graphite, carbon black and coal powders in the ranges of X-band frequencies (8.2 to 12.4 GHz) and between 1 and 10 GHz. ISIJ Int 2011;51:1766–72.

[26] Mirzaee M, Noghanian S, Wiest L, Chang I. Developing flexible 3D printed antenna using conductive ABS materials. In: 2015 IEEE International Symposium on Antennas and Propagation & USNC/URSI National Radio Science Meeting. IEEE, 2015.
[27] Yurduseven O, Flowers P, Ye S, et al. Computational microwave imaging using 3D printed conductive polymer frequency-diverse metasurface antennas. IET Microw Antenna P 2017;11:1962–9.
[28] Chizari K, Arjmand M, Liu Z, Sundararaj U, Therriault D. Three-dimensional printing of highly conductive polymer nanocomposites for EMI shielding applications. Mater Today Commun 2017;11:112–8.
[29] Yang H, Leow WR, Wang T, et al. 3D printed photoresponsive devices based on shape memory composites. Adv Mater 2017;29:1701627.
[30] Kuang X, Chen K, Dunn CK, Wu J, Li VCF, Qi HJ. 3D printing of highly stretchable, shape-memory, and self-healing elastomer toward novel 4D printing. ACS Appl Mater Interfaces 2018;10:7381–8.
[31] Huang L, Jiang R, Wu J, et al. Ultrafast digital printing toward 4D shape changing materials. Adv Mater 2017;29:1605390.
[32] Saed MO, Ambulo CP, Kim H, et al. Molecularly-engineered, 4D-printed liquid crystal elastomer actuators. Adv Funct Mater 2019;29:1806412.
[33] López-Valdeolivas M, Liu D, Broer DJ, Sánchez-Somolinos C. 4D printed actuators with soft-robotic functions. Macromol Rapid Commun 2018;39:1700710.
[34] Kuang X, Roach DJ, Wu J, et al. Advances in 4D printing: materials and applications. Adv Funct Mater 2019;29:1805290.
[35] Momeni F, Liu X, Ni J. A review of 4D printing. Mater Design 2017;122:42–79.
[36] Leist SK, Zhou J. Current status of 4D printing technology and the potential of light-reactive smart materials as 4D printable materials. Virtual Phys Prototy 2016;11:249–62.
[37] Barrio JD, Sánchez-Somolino C. Light to shape the future: from photolithography to 4D printing. Adv Mater Technol 2019;7:1900598.
[38] Zhang Q, Yan D, Zhang K, Hu G. Pattern transformation of heat-shrinkable polymer by three-dimensional (3D) printing technique. Sci Rep 2015;5:8936.
[39] Zhang Q, Zhang K, Hu G. Smart three-dimensional lightweight structure triggered from a thin composite sheet via 3D printing technique. Sci Rep 2016;6:22431.
[40] Bi H, Xu M, Ye G, Guo R, Cai L, Ren Z. Mechanical, thermal, and shape memory properties of three-dimensional printing biomass composites. Polymers 2018;10:1234.
[41] Monzón MD, Paz R, Pei E, et al. 4D printing: processability and measurement of recovery force in shape memory polymers. Int J Adv Manuf Tech 2017;89:1827–36.
[42] Ge Q, Dunn CK, Qi HJ, Dunn ML. Active origami by 4D printing. Smart Mater Struct 2014;23:094007.
[43] Zarek M, Layani M, Cooperstein I, Sachyani E, Cohn D, Magdassi S. 3D printing of shape memory polymers for flexible electronic devices. Adv Mater 2016;28:4449–54.
[44] Raviv D, Zhao W, McKnelly C, et al. Active printed materials for complex self-evolving deformations. Sci Rep 2014;4:7422.
[45] Bakarich SE, Gorkin III R, Panhuis MIH, Spinks GM. 4D printing with mechanically robust, thermally actuating hydrogels. Macromol Rapid Commun 2015;36:1211–7.
[46] Zheng SY, Shen Y, Zhu F, et al. Programmed deformations of 3D-printed tough physical hydrogels with high response speed and large output force. Adv Funct Mater 2018;28:1803366.
[47] Naficy S, Gately R, Gorkin III R, Xin H, Spinks GM. 4D printing of reversible shape morphing hydrogel structures. Macromol Mater Eng 2017;302:1600212.
[48] Gladman AS, Matsumoto EA, Nuzzo RG, Mahadevan L, Lewis JA. Biomimetic 4D printing. Nat Mater 2016;15:413.
[49] Yuan C, Roach DJ, Dunn CK, et al. 3D printed reversible shape changing soft actuators assisted by liquid crystal elastomers. Soft Matter 2017;13:5558–68.
[50] Ambulo CP, Burroughs JJ, Boothby JM, Kim H, Shankar MR, Ware TH. Four-dimensional printing of liquid crystal elastomers. ACS Appl Mater Interfaces 2017;9:37332–9.
[51] Kotikian A, Truby RL, Boley JW, White TJ, Lewis JA. 3D printing of liquid crystal elastomeric actuators with spatially programed nematic order. Adv Mater 2018;30:1706164.
[52] Salazar-Serrano LJ, Torres JP, Valencia A. A 3D printed toolbox for opto-mechanical component. PLoS One 2017;12: e0169832.
[53] Kaur A, Myers JC, Ghazali MIM, Byford J, Chahal P. Affordable terahertz components using 3D printing. In: IEEE 65th Electronic Components and Technology Conference, 2015.
[54] Iezzi VL, Boisvert J, Loranger S, Kashyap R. 3D printed long period gratings for optical fibers. Opt Lett 2016;8:1865–68.
[55] Squires AD, Constable E, Lewis RA. 3D printed terahertz diffraction gratings and lenses. J Infrared Milli Terahz Waves 2015;36:72–80.
[56] Garrard K, Bruegge T, Hoffman J, Dow T, Sohn A. Design tools for freeform optics. In: Current developments in lens design and optical engineering VI, International Society for Optics and Photonics, 2005.
[57] Fang F, Cheng Y, Zhang X. Design of freeform optics. Adv Opt Technol 2013;2:445–53.
[58] Davenport TLR. 3D NURBS representation of surfaces for illumination. In: International Optical Design Conference 2002, International Society for Optics and Photonics, 2002.
[59] Cassarly WJ, Hayford MJ. Illumination optimization: the revolution has begun. In: International Optical Design Conference 2002, International Society for Optics and Photonics, 2002.
[60] Kaya I, Rolland JP. A radial basis function method for freeform optics surfaces. In: Frontiers in Optics, Optical Society of America, 2010.
[61] Herkommer AM. Advances in the design of freeform systems for imaging and illumination applications. J Opt 2014;43:261–8.
[62] Brix K, Hafizogullari Y, Platen A. Designing illumination lenses and mirrors by the numerical solution of Monge–Ampère equations. JOSA A 2015;32:2227–36.
[63] An HS, Park YG, Kim K, Nam YS, Song MH, Park JU. High-resolution 3D printing of freeform, transparent displays in ambient air. Adv Sci 2019;1901603.
[64] Willis K, Brockmeyer E, Hudson S, Poupyrev I. Printed optics:3D printing of embedded optical elements for interactive devices. In: Proceedings of the 25th annual ACM symposium on User interface software and technology. Washington, DC, USA, ACM, 2012.
[65] Hull CW. Apparatus for production of three-dimensional objects by stereolithography. Google Patents, 1986.
[66] Chen M, Zhong M, Johnson JA. Light-controlled radical polymerization: Mechanisms, methods, and applications. Chem Rev 2016;116:10167–211.
[67] Pan X, Tasdelen MA, Laun J, Junkers T, Yagci Y, Matyjaszewski K. Photomediated controlled radical polymerization. Prog Polym Sci 2016;62:73–125.
[68] Shi S, Croutxe-Barghorn C, Allonas X. Photoinitiating systems for cationic photopolymerization: Ongoing push toward

long wavelengths and low light intensities. Prog Polym Sci 2017;65:1–41.
[69] Zhou F, Cao W, Dong B, Reissman T, Zhang W, Sun C. Additive manufacturing of a 3D terahertz gradient-refractive index lens. Adv Opt Mater 2016;4:1034–40.
[70] Bártolo PJ. Stereolithography: materials, processes and applications. Berlin, Germany: Springer Science & Business Media, 2011.
[71] Vaidya N, Solgaard O. 3D printed optics with nanometer scale surface roughness. Microsyst Nanoeng 2018;4:18.
[72] Gissibl T, Thiele S, Herkommer A, Giessen H. Sub-micrometre accurate free-form optics by three-dimensional printing on single-mode fibres. Nat Commun 2016;7:11763.
[73] Thiele S, Arzenbacher K, Gissibl T, Giessen H, Herkommer AM. 3D-printed eagle eye: Compound microlens system for foveated imaging. Sci Adv 2017;3:e1602655.
[74] Juodkazis S. Manufacturing: 3D printed micro-optics. Nat Photonics 2016;10:499.
[75] Lim J, Kim YK, Won D, Choi IH, Lee S, Kim J. 3D printing of free-standing overhanging structures utilizing an in situ light guide. Adv Mater Technol 2019;4:1900118.
[76] Park SH, Su R, Jeong J, et al. 3D printed polymer photodetectors. Adv Mater 2018;30:1803980.
[77] Davies MA, Evans CJ, Vohra RR, Bergner BC, Patterson SR. Application of precision diamond machining to the manufacture of microphotonics components. In: Lithographic and micromachining techniques for optical component fabrication II, International Society for Optics and Photonics, 2003.
[78] Kotz F, Arnold K, Bauer W, et al. Three-dimensional printing of transparent fused silica glass. Nature 2017;544:337.
[79] Udofia EN, Zhou W. 3D Printed optics with a soft and stretchable optical material. Addit Manuf 2020;31:100912.
[80] Maruo S, Fourkas JT. Recent progress in multiphoton microfabrication. Laser Photonics Rev 2008;2:100–11.
[81] Nguyen HHD, Hollenbach U, Ostrzinski U, Pfeiffer K, Hengsbach S, Mohr J. Freeform three-dimensional embedded polymer waveguides enabled by external-diffusion assisted two-photon lithography. Appl Opt 2016;55:1906–12.
[82] Williams HE, Freppon DJ, Kuebler SM, Rumpf RC, Melino MA. Fabrication of three-dimensional micro-photonic structures on the tip of optical fibers using SU-8. Opt Express 2011;19:22910–22.
[83] Sokolovskii GS, Melissinaki V, Dudelev VV, et al. Superfocusing of high-M2 semiconductor laser beams: experimental demonstration. In: Semiconductor Lasers and Laser Dynamics VI, International Society for Optics and Photonics, 2014.
[84] Melissinaki V, Konidakis I, Farsari M, Pissadakis S. Fiber endface fabry–perot microsensor with distinct response to vapors of different chlorinated organic solvents. IEEE Sens J 2016;16:7094–100.
[85] Maruo S, Kawata S. Two-photon-absorbed near-infrared photopolymerization for three-dimensional microfabrication. J Microelectromech Syst 1998;7:411–5.
[86] Hahn V, Mayer F, Thiel M, Wegener M. 3-D laser nanoprinting. Opt Photonics News 2019;30:28–35.
[87] Gissibl T, Thiele S, Herkommer A, Giessen H. Two-photon direct laser writing of ultracompact multi-lens objectives. Nat Photonics 2016;10:554.
[88] Pyo J, Kim JT, Lee J, Yoo J, Je JH. 3D printed nanophotonic waveguides. Adv Opt Mater 2016;4:1190–5.
[89] Guo R, Li Z, Jiang Z, Yuan D, Huang W, Xia A. Log-pile photonic crystal fabricated by two-photon photopolymerization. J Opt A: Pure Appl Opt 2005;7:396.
[90] Farsari M, Chichkov BN. Materials processing: Two-photon fabrication. Nat Photonics 2009;3:450.
[91] Xiong X, Xue Z-H, Meng C, et al. Polarization-dependent perfect absorbers/reflectors based on a three-dimensional metamaterial. Phys Rev B 2013;88:115105.
[92] Fischer J, Ergin T, Wegener M. Three-dimensional polarization-independent visible-frequency carpet invisibility cloak. Opt Lett 2011;36:2059–61.
[93] Ergin T, Stenger N, Brenner P, Pendry JB, Wegener M. Three-dimensional invisibility cloak at optical wavelengths. Science 2010;328:337–9.
[94] Xin H, Liang M. 3-D-printed microwave and THz devices using polymer jetting techniques. Proc IEEE 2017;105:737–55.
[95] Gospodaric J, Kuzmenko A, Pimenov A, et al. 3D-printed phase waveplates for THz beam shaping. Appl Phys Lett 2018;112:221104.
[96] Hernandez-Serrano A, Sun Q, Bishop EG, et al. Design and fabrication of 3-D printed conductive polymer structures for THz polarization control. Opt Express 2019;27:11635–41.
[97] Garcia CR, Correa J, Espalin D, et al. 3D printing of anisotropic metamaterials. Prog Electromagn Res 2012;34:75–82.
[98] Grant PS, Castles F, Lei Q, et al. Manufacture of electrical and magnetic graded and anisotropic materials for novel manipulations of microwaves. Phil Trans R Soc A 2015;373:20140353.
[99] Ishikawa A, Kato T, Takeyasu N, Fujimori K, Tsuruta K. Selective electroless plating of 3D-printed plastic structures for three-dimensional microwave metamaterials. Appl Phys Lett 2017;111:183102.
[100] Isakov D, Stevens CJ, Castles F, Grant PS. 3D-printed high dielectric contrast gradient index flat lens for a directive antenna with reduced dimensions. Adv Mater Technol 2016;1:1600072.
[101] Chen J, Yuan X, Chen M, et al. Ultrabroadband three-dimensional printed radial perfectly symmetric gradient honeycomb all-dielectric dual-directional lightweight planar Luneburg lens. ACS Appl Mater Interfaces 2018;10:38404–9.
[102] Liang M, Ng WR, Chang K, Gbele K, Gehm ME, Xin H. A 3-D Luneburg lens antenna fabricated by polymer jetting rapid prototyping. IEEE Trans Antennas Propag 2014;62:1799–807.
[103] Yi J, Burokur SN, Piau G-P, de Lustrac A. 3D printed broadband transformation optics based all-dielectric microwave lenses. J Opt 2016;18:044010.
[104] Castles F, Isakov D, Lui A, et al. Microwave dielectric characterisation of 3D-printed $BaTiO_3$/ABS polymer composites. Sci Rep 2016;6:22714.
[105] Isakov DV, Lei Q, Castles F, Stevens CJ, Grovenor CRM, Grant PS. 3D printed anisotropic dielectric composite with metamaterial features. Mater Design 2016;93:423–430.
[106] Wang Y, Castles F, Grant PS. 3D printing of NiZn ferrite/ABS magnetic composites for electromagnetic devices. MRS Online Proceedings Library Archive 2015;1788:29–35.
[107] Xie Y, Ye S, Reyes C, et al. Microwave metamaterials made by fused deposition 3D printing of a highly conductive copper-based filament. Appl Phys Lett 2017;110:181903.
[108] Ehrenberg IM, Sarma SE, Wu B-I. A three-dimensional self-supporting low loss microwave lens with a negative refractive index. J Appl Phys 2012;112:073114.

[109] Park HS, Kim TT, Kim HD, Kim K, Min B. Nondispersive optical activity of meshed helical metamaterials. Nat Commun 2014;5:5435.
[110] Jensen JS, Sigmund O. Topology optimization for nanophotonics. Laser Photonics Rev 2011;5:308–21.
[111] Piggott AY, Lu J, Lagoudakis KG, Petykiewicz J, Babinec TM, Vučković J. Inverse design and demonstration of a compact and broadband on-chip wavelength demultiplexer. Nat Photonics 2015;9:374.
[112] Molesky S, Lin Z, Piggott AY, Jin W, Vucković J, Rodriguez AW. Inverse design in nanophotonics. Nat Photonics 2018;12:659–70.
[113] Callewaert F, Butun S, Li Z, Aydin K. Inverse design of an ultra-compact broadband optical diode based on asymmetric spatial mode conversion. Sci Rep 2016;6:32577.
[114] Lu J, Vučković J. Inverse design of nanophotonic structures using complementary convex optimization. Opt Express 2010;18:3793–804
[115] Lu J, Vučković J. Objective-first design of high-efficiency, small-footprint couplers between arbitrary nanophotonic waveguide modes. Opt Express 2012;20:7221–36.
[116] Diest K. Numerical methods for metamaterial design. Berlin, Germany: Springer, 2013.
[117] Callewaert F, Velev V, Jiang S, Sahakian AV, Kumar P, Aydin K. Inverse-designed stretchable metalens with tunable focal distance. Appl Phys Lett 2018;112:091102.
[118] Estakhri NM, Edwards B, Engheta N. Inverse-designed metastructures that solve equations. Science 2019;363: 1333–8.
[119] Callewaert F, Velev V, Kumar P, Sahakian AV, Aydin K. Inverse-designed broadband all-dielectric electromagnetic metadevices. Sci Rep 2018;8:1358.
[120] Wei H, Callewaert F, Hadibrata W, et al. Two-photon direct laser writing of inverse-designed free-form near-infrared polarization beamsplitter. Adv Opt Mater 2019;1900513.
[121] Flatae AM, Burresi M, Zeng H, et al. Optically controlled elastic microcavities. Light Sci Appl 2015;4:e282.
[122] Zeng H, Martella D, Wasylczyk P, et al. High-resolution 3D direct laser writing for liquid-crystalline elastomer microstructures. Adv Mater 2014;26:2319–22.
[123] Nocentini S, Martella D, Parmeggiani C, Zanotto S, Wiersma DS. Structured optical materials controlled by light. Adv Opt Mater 2018;6:1800167.
[124] De Bellis I, Martella D, Parmeggiani C, et al. Modulation of optical properties in liquid crystalline networks across different length scales. J Phys Chem C 2019;123:26522–7.
[125] Kumar GS, Neckers DC. Photochemistry of azobenzene-containing polymers. Chem Rev 1989;89:1915–25.
[126] Szukalski A, Uttiya S, D'Elia F, et al. 3D photo-responsive optical devices manufactured by advanced printing technologies. In: Organic Photonic Materials and Devices XXI. International Society for Optics and Photonics, 2019.
[127] Nocentini S, Riboli F, Burresi M, Martella D, Parmeggiani C, Wiersma DS. Three-dimensional photonic circuits in rigid and soft polymers tunable by light. ACS Photonics 2018;5:3222–30.
[128] Kim Y, Tamaoki N. Asymmetric dimers of chiral azobenzene dopants exhibiting unusual helical twisting power upon photoswitching in cholesteric liquid crystals. ACS Appl Mater Interfaces 2016;8:4918–26.
[129] Lu HB, Xie XY, Xing J, et al. Wavelength-tuning and band-broadening of a cholesteric liquid crystal induced by a cyclic chiral azobenzene compound. Opt Mater Express 2016;6:3145–58.
[130] Ryabchun A, Raguzin I, Stumpe J, Shibaev V, Bobrovsky A. Cholesteric polymer scaffolds filled with azobenzene-containing nematic mixture with phototunable optical properties. ACS Appl Mater Interfaces 2016;8:27227–35.
[131] Ryu SH, Gim M-J, Lee W, Choi S-W, Yoon DK. Switchable photonic crystals using one-dimensional confined liquid crystals for photonic device application. ACS Appl Mater Interfaces 2017;9:3186–91.
[132] Scarpa E, Lemma ED, Fiammengo R, et al. Microfabrication of pH-responsive 3D hydrogel structures via two-photon polymerization of high-molecular-weight poly (ethylene glycol) diacrylates. Sensor Actuat B:Chem 2019;279:418–26.
[133] Tudor A, Delaney C, Zhang H, et al. Fabrication of soft, stimulus-responsive structures with sub-micron resolution via two-photon polymerization of poly (ionic liquid) s. Mater Today 2018;21:807–16.
[134] Lu D-X, Zhang Y-L, Han D-D, et al. Solvent-tunable PDMS microlens fabricated by femtosecond laser direct writing. J Mater Chem C 2015;3:1751–6.
[135] An SC, Lee E, Lee CH, et al. Sharp Fano Resonance and Spectral Collapse in Stimuli-Responsive Photonic Structures. Adv Opt Mater 2019;7:1801206.
[136] Sweeney M, Acreman M, Vettese T, Myatt R, Thompson M. Application and testing of additive manufacturing for mirrors and precision structures. In: Material Technologies and Applications to Optics, Structures, Components, and Sub-Systems II, International Society for Optics and Photonics, 2015.
[137] Sigel A, Merkel M, Heinrich A. Miniaturization of an optical 3D sensor by additive manufacture of metallic mirrors. In: Optical Measurement Systems for Industrial Inspection X, International Society for Optics and Photonics, 2017.
[138] Skylar-Scott MA, Gunasekaran S, Lewis JA. Laser-assisted direct ink writing of planar and 3D metal architectures. Proc Natl Acad Sci USA 2016;113:6137–42.
[139] Khattak HK, Bianucci P, Slepkov AD. Linking plasma formation in grapes to microwave resonances of aqueous dimers. Proc Natl Acad Sci USA 2019;116:4000–5.
[140] Kelly BE, Bhattacharya I, Heidari H, Shusteff M, Spadaccini CM, Taylor HK. Volumetric additive manufacturing via tomographic reconstruction. Science 2019;363:1075–9.
[141] Walker DA, Hedrick JL, Mirkin CA. Rapid, large-volume, thermally controlled 3D printing using a mobile liquid interface. Science 2019;366:360–4.